DOE Award No.: DF-FG02-08ER15990

Predictive Models of CO_2 Sequestration Dynamics Based on Multiscale Experiments and Theoretical Analysis

Final Report

A. R. Kovscek[1], H. A. Tchelepi[1],

F. G. Gibou[2] and E. H. Meiburg[2],

2011

[1]Department of Energy Resources Engineering, Green Earth Sciences BLDG, room 065, Stanford, CA 94305-2220.
[2]Department of Mechanical Engineering, Engineering II Bldg., University of California, Santa Barbara, CA 93106-5070.

Executive Summary

CO_2 sequestration operations in deep subsurface geologic formations involve complex multiphase interactions that are not fully understood. This research project was aimed at developing such an understanding with focus on the detailed pore-scale physics and the development of a framework to translate the pore-scale physics to the Darcy and larger scales. The project had substantial experimental and computational components. The experiments focused on the use of micromodels. Drainage experiments of immiscible two-phase flow were performed. The viscosity ratio, M, varied from highly favorable ($M = 0.3$) to highly unfavorable ($M = 84$). For each viscosity ratio, the capillary-number, C_a, was varied across a wide range. The experiments show that when M is much larger than unity, the flow patterns are quite complex with a wide range of finger length scales. Overall, for a given $M > 1$, the instabilities associated with these immiscible displacements are more benign than their miscible counterparts. Specifically, unlike the miscible setting, immiscible instabilities are rarely dominated by of a few large fingers that bypass the resident fluid. However, the local wetting phase saturation in the flooded regions can be persistently large indicating significant microscopic bypassing. The standard Darcy model for multiphase flow cannot fully capture these observations. In addition to the multiscale nature of multiphase flows in porous media, the complex geometry of the porous medium and the complex fluid-fluid and fluid-solid interface pose serious modeling and computational challenges. Existing Lattice-Boltzmann models have not been designed to describe the complex solid-fluid and immiscible fluid-fluid contacts, and we decided to employ alternative strategies. To better understand the fluid-flow physics at the pore scale, we employed a level-set method that keeps track of the interface between the two immiscible fluids along with implicit representation of the pore-scale geometry. 'Sharp' conditions at the contact-lines between fluids and at the solid boundaries were employed. The Octree adaptive mesh refinement framework was extended in order to solve this immiscible two-phase problem with reasonably good resolution. Computational results of the effects of capillary, viscous, and gravitational forces have been performed. Validation of our level-set approach for complex pore-scale rock geometries is ongoing. We also developed novel numerical methods for the pressure equation associated with the Navier-Stokes momentum balance. The formulation, which is obtained using a mass weighted continuity equation, ensures a locally conservative velocity field. The jump conditions of pressure and the normal viscous stresses and the continuity of the interfacial stresses are enforced at fluid-fluid interfaces. Solid boundaries are treated using an immersed boundary method.

We have also been developing mathematical and computational approaches to translate the physics of immiscible two-phase flow in the presence of viscosity and density differences from the pore to the Darcy scale. Since a modeling framework will ultimately be necessary in order to design and manage large-scale sequestration projects, there is an urgent need to develop models and constitutive relations that describe the relevant multiscale physics accurately. The experimental findings and the advanced computational methods developed in this research project provide a strong basis for designing and validating constitute relations and models of multiphase flow at the pore and larger (e.g., Darcy) scales.

Introduction

A fundamental understanding of multiphase, immiscible, unstable fluid flow in natural porous media across a range of length and time scales is essential to describe the behaviors associated with CO_2 sequestration in geological saline formations. The characteristics of two phase immiscible flow dynamics depend on capillary, viscous, and gravitational forces. Current challenges involved in understanding multiphase flow dynamics include the heterogeneous and multiscale nature of geological porous media and the enormous difficulties in fully characterizing their properties. The significant differences in density and viscosity between super-critical CO_2 and the resident fluid (brine) leads to unstable flow dynamics. Conventional modeling of the CO_2 injection process is based on a Darcy law formulation that assumes stable and uniform flows that are in local equilibrium throughout the system. During the injection phase of sequestration operations, it might not be appropriate to apply Darcy-based modeling due to the likelihood of an unstable flow displacement. During the post-injection period, the evolution of gravity currents in large-scale deep formations may involve complex immiscible and miscible convective instabilities that dictate the overall migration patterns of the CO_2 plumes.

Despite all the work conducted to characterize unstable multiphase flow processes, there is a lack of predictive modeling capabilities for CO_2 sequestration in geological formations that is verified using multiscale experimental data. The flow of fluids in natural porous media is fundamentally a microscopic process that must be represented across a hierarchy of scales relevant to sequestration. Our objectives were to investigate the relevant physical mechanisms at the microscopic (pore) and mesoscopic (Darcy) scales with the help of detailed micromodel experiments and high-accuracy numerical simulations.

The experimental work with emphasis on unstable immiscible two-phase drainage displacements is described in the next chapter. Then, the level-set method for modeling two-phase flow at the pore scale is described, and that is followed by a brief description of novel methods to obtain a conservative pore-scale velocity field, as well as, preliminary results of a volume-averaging approach to translate the multiphase flow dynamics to the Darcy scale.

Micromodel Investigation of Viscously Unstable Displacement

Introduction

Flow in porous media is fundamentally a microscopic process. Once the pore-scale physics of multi-component multiphase fluid flow is understood fully and modeled accurately, the dynamics must then be translated across a hierarchy of scales. Accordingly, the experimental investigation focused on the pore scale. Our experimental objectives were to

1. investigate the physical mechanisms occurring at the pore-scale, specifically viscous, capillary, and gravitational forces and their effect on the flow regimes and

2. develop a methodology for quantitative analysis of experimental data.

The experiments focused on exploring the effect of unfavorable viscosity ratios, capillary numbers, and gravitational forces on the flow dynamics of unstable drainage processes where brine was the defending phase. The experimental work employs analogous fluid pairs for drainage experiments in etched-silicon micromodels. Much of the experimental design fluid selection was based on the work of Cinar et al. (8) who conducted experiments in glass beadpacks. The experimental data are analyzed through image analysis at the pore and ensemble network scales. Current results have shown a stable displacement under favorable viscosity conditions. Under unfavorable mobility conditions, viscous fingering and a weakly-organized front have been recorded.

The experimental section proceeds with a description of the apparatus, methods, and fluid pairs studied. Preliminary results are then presented to illustrate the problems that arose with image contrast and image analysis. Significant effort was then expended to improve image contrast. Results with improved contrast are then presented and discussed.

Apparatus

The experimental apparatus utilized for this research includes, liquid chromatography pumps that provide low velocity oscillation-free pumping, piston-cylinder fluid transfer vessels, optical equipment, and the micromodel itself. A system diagram representing the overall experimental setup is presented in Fig. 1. Both drainage

and imbibition experiments were conducted, therefore, the exact arrangement of the pump-piston-bomb system is slightly different depending on the experiment. The details of each component are discussed in the following subsections.
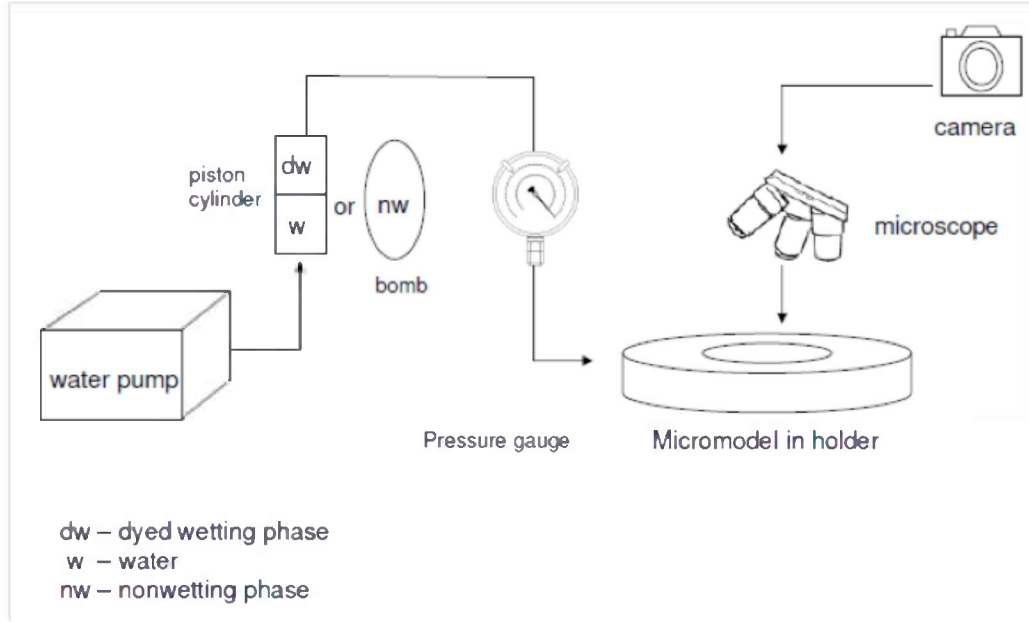

Figure 1: The experimental apparatus.

Micromodel

Micromodels contain a pore-network pattern etched onto a silicon wafer. Although they are limited to two-dimensions, micromodels provide the best methodology to visualize directly pore-scale flow. The maximum pressure that our micromodels can withstand without a specially designed pressure vessel is approximately 60 psi. Therefore, the experiments are conducted in a relatively low-pressure system. The dimensions of the micromodels are 5 by 5 cm with 25 μm etch depth. Figure 2 is an image of a whole micromodel. Each model reflects a two-dimensional porous medium of 600 by 600 pores. This number of pores is sufficient to meet the scaling requirements for representative elementary volume. As shown in Fig. 2 by the red circle, there are two etched inlet/outlet ports at each corner of the pore network, allowing the fluid to enter and exit the network.

The silicon wafers used to make the micromodels were created using a mask to form the etched network. Standard photolithography tools were used. The design of the mask is representative of sedimentary rock. Figure 3 illustrates a small portion of the etched-network pattern. In this study, micromodel pore network contains a topology that is very similar to Berea sandstone. The properties associated with the micromodel produced from this mask are listed in Table 1. The permeability of the micromodels was measured to be approximately 1 Darcy (?).
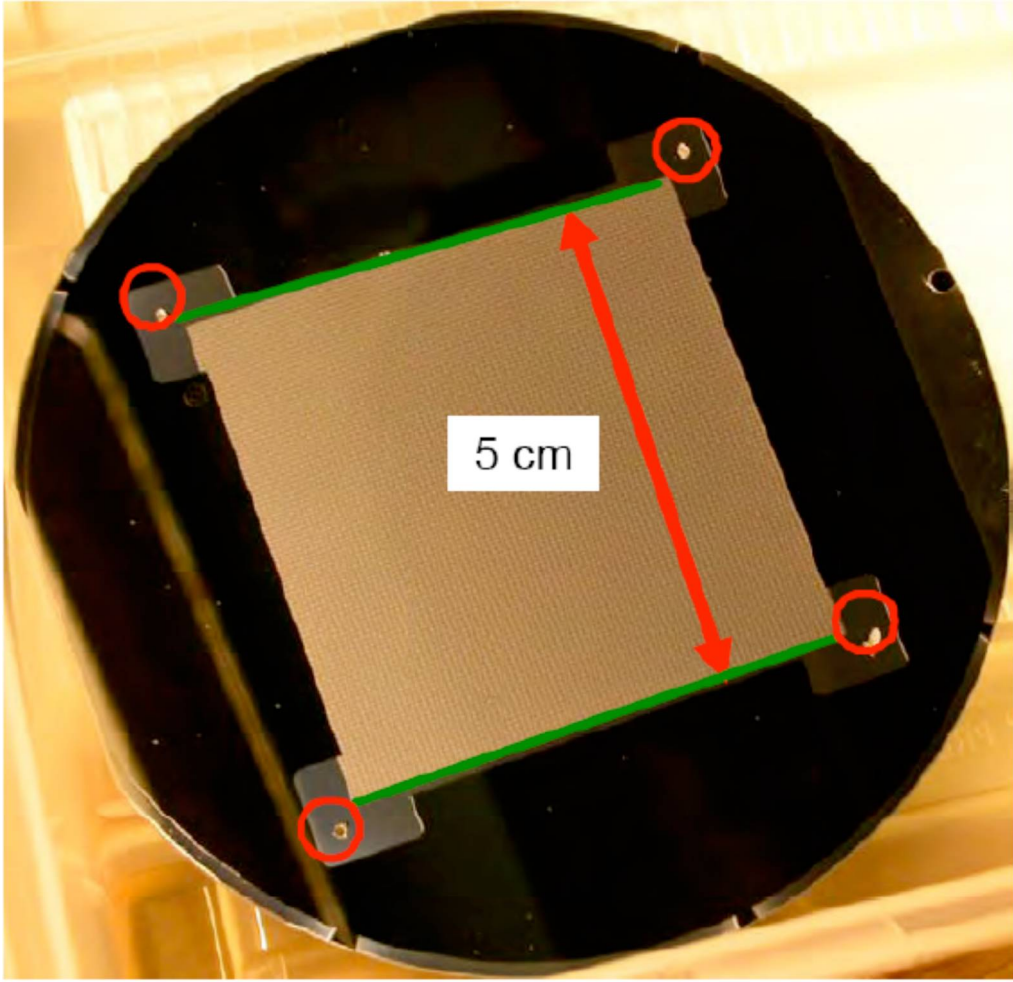
Figure 2: Photograph of an etched silicon micromodel outside of holder. The red circles show the location of fluid entry and exit points. The green lines show the position of fluid distribution and collection channels along the edge of the micromodel

Table 1: Micromodel properties.

grain size	30 to 300 μm
porosity	47 %
pore volume	0.029 cm^3
dimensions	5 by 5 cm
unit cell dimensions	480 by 400 μm
etched depth	25 μm
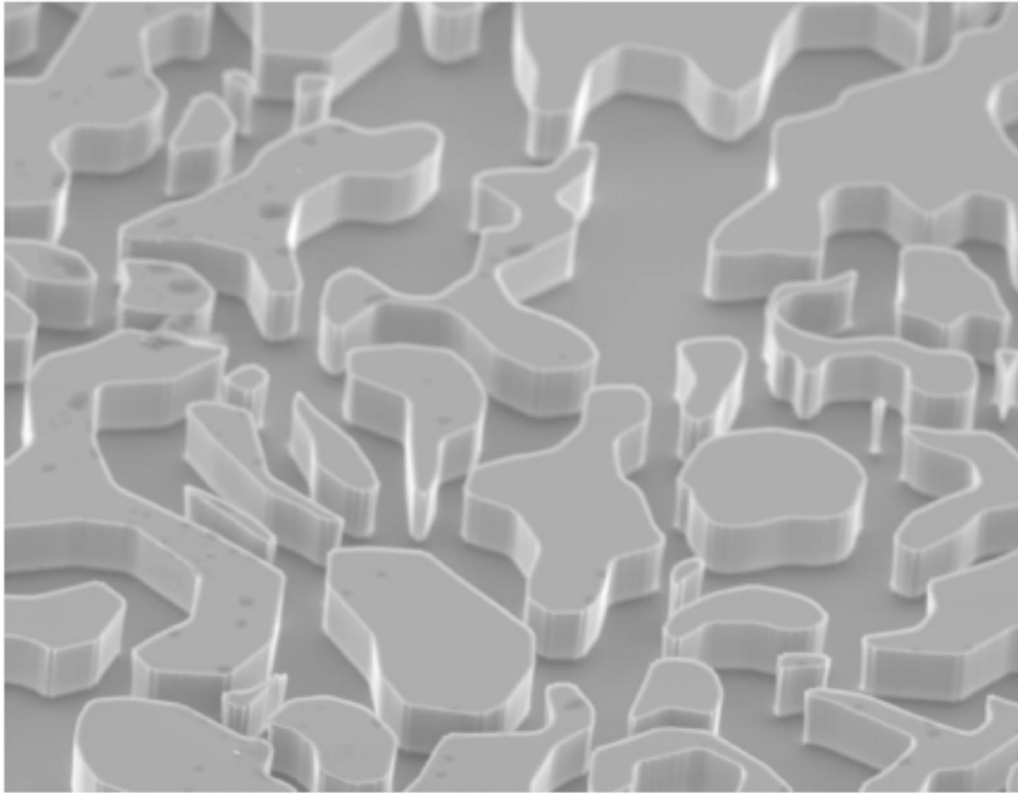
Figure 3: Scanning electron microscope image of the etched network pattern of the silicon micro-model.

The silicon wafers were cleaned and etched at the Stanford Nanofabrication Facility (SNF). The steps involved in the fabrication starts with the imaging of the model onto the silicon wafer. This step involves the digitization of a rock section into a computer, for example see Rangel German and Kovscek (27) and references therein. The image is then replicated on a chrome or glass mask. Silicon wafers are uniformly coated with photoresist. Flow path image is created by exposing the wafer with an ultraviolet ray through the mast onto the wafer. After the unexposed photoresist is removed, deep etching is done to the exposed silicon wafer using a dry etch technique. Four holes are drilled through each corner of the etched silicon wafers and they were cleaned using 9:1 H_2SO_4 : H_2O_2 solution (15).

Upon the completion of silicon wafer etching, holes are drilled into the fluid access ports, as shown the circled areas in Fig. 2. The etched-pore pattern is sealed by a glass plate. The apparatus used for micromodel bonding consists of a hot plate, voltage source, and voltage plate. The side with the etched network of a silicon wafer is anodically bonded to a glass plate in order to form a complete micromodel. During the anodic bonding, the surfaces of the silicon wafer and glass plate are put in contact where the silicon wafer is placed on an anode, the glass plate rests on top of the silicon wafer, and a cathode is placed on top of the glass plate. The hot plate is preheated to 350°C and the silicon wafer is placed on the plate for 45 minutes. During this time the surfaces of the silicon wafers are exposed to the air at high temperature, and therefore oxidized to SiO_2. Then, the glass plate is placed on top of the silicon wafer for 2 minutes while letting the hot plate temperature drop to 300°C. The voltage plate is then placed on top of the glass plate and provides a voltage supply at 1200 volts. After 60 minutes the electricity is turned off and the new micromodel is allowed to cool to room temperature.

The complete micromodel is placed into an aluminum holder (Fig. 4) and 2 entry and exit ports of the micromodels are connected to the injection and production systems. Figure 4 part (A) shows the bottom piece of the micromodel holder where 4 part (B) shows the placement of o-ring in the holder. The micromodel has a pore volume of 0.041 ml, shown in Table 1. It is important to estimate the additional space taken by the micromodel holder ports. Each entry port in the aluminum holder takes up a volume of approximately 0.1 mL (1). This leads to a total volume of 0.061 cm^3. Furthermore, the fracture and o-ring (4 part (B)) also have to be filled as fluids are injected into the porous media. The volume of these two sections is estimated to be around 0.1-0.2 cm^3. The uncertainties of the total port volumes makes it difficult to calculate pore volume injected as well as to perform typical volumetric calculations such as the fluid displaced.

Optics

A Nikon Eclipse ME 600 microscope with a photo tube that connects to a video camera was employed to visualize the flow pattern at the pore level in the micromodel. It provides a magnified image of the micromodel at 40X, 100X, and 200X. The silicon wafer micromodels are opaque and they were monitored using reflected light. The microscope has an internal light source. A Nikon Coolpix P5100 was connected to
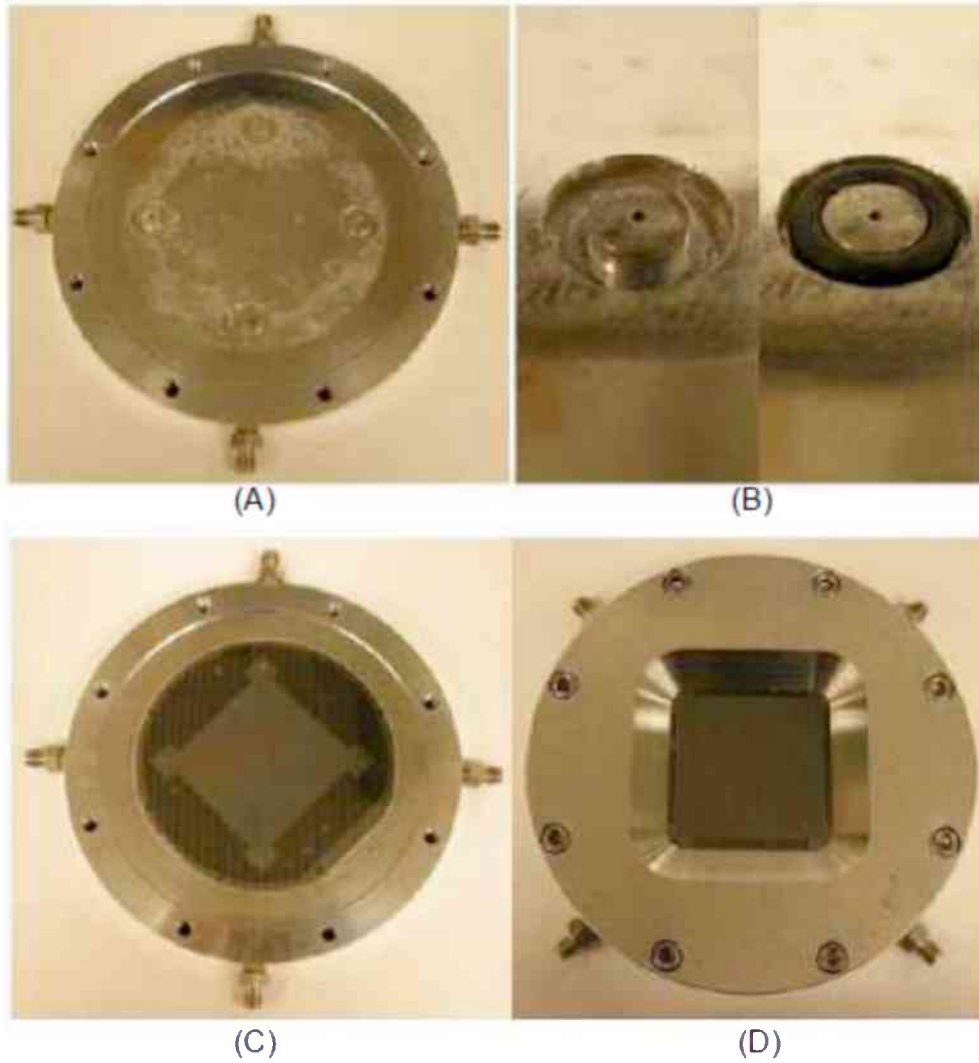
Figure 4: Complete micromodel setup. (A) The bottom of the holder (B) The placement of o-ring (C) The placement of micromodel onto the holder and (D) Complete micromodel.

the photo tube. High definition micromodel images at the pore-level were collected using the video camera. Macroscopic images and videos showing time-lapse pore level events were also captured.

Illumination is obtained using white light obtained by a halogen lamp in a standard microscope light source. Alternative lighting is provided by an ultraviolet (UV) light source. It is a fluorescent ring with UV light (Aven 26200B-203) in the range of wavelengths from 340 to 360 nm. The ring mounts on the microscope objective and illuminates the micromodel below.

Pumps and fluid transfer

A Teledyne ISCO 100D syringe pump was used to inject fluids and push the immiscible displacement through the micromodel. The pump was configured to maintain a constant volumetric flow rate during the drainage and imbibition processes. The pump also delivers a pressure reading; however, due to the lack of accuracy, a pressure gauge was connected between the pump and the micromodel to obtain the inlet pressure information. During the cleaning process, toluene was used to flood the micromodel followed by isopropanol using an LC-2600 syringe pump under constant pressure (around 10 psi).

For two-phase drainage displacements, distilled water was pumped to push the wetting phase of interest. Because distilled water and the wetting phase fluids are miscible, it is necessary to separate these two fluids. A stainless steel piston-cylinder transfer vessel (approximately 200 ml in volume) was made in the Stanford Mechanical Engineering Machine Shop.

Experimental Procedures

The overall experimental system is presented in Fig. 1. The water from the pump pushes dyed water in the piston or nonwetting phase in the bomb through the micromodel pore network. A pressure gauge is connected between the bomb and micromodel holder to measure the inlet pressure. The flow pattern and fluid distribution as well as interfaces between the two phases are observed and captured with the microscope and the video camera.

Fluid preparation and characterization

The first step of the experiment is the preparation and characterization of the fluid systems. Fluid pairs were prepared to achieve a range of viscosity ratios and produce either stable or unstable drainage displacement. For the stable drainage displacement, hexadecane was selected as the nonwetting phase and house-distilled water was selected as the wetting phase. For the unstable drainage displacement, a mixture of glycerol and water represented the wetting phase while n-heptane was used for non-wetting, displacing phase.

Because both the wetting and nonwetting fluids are clear, it was necessary to use a fluid dye to enhance the contrast between the phases. Various trials were made

in which the wetting and the nonwetting phase were dyed. Two dyes were used extensively in this study. First, a green dye (Brilliant Green by Hartman-Leddon Co.) was selected to dye the injected wetting phase (0.5 wt%). Second, an ultraviolet (UV) light sensitive dye was used at a concentration of 1 vol%. The trade name of the UV dye is "Visible Fluorescent Water Based Tracer" (Black Light World).

Various combinations of fluid mixtures were used such as hexadecane/distilled water, glycerol, distilled water and n-heptane with equal weights , and glycerol (44wt%), distilled water (23wt%) and n-heptane (33wt%). Fluid pairs were pre-equilibrated and characterized before the experiments. The steps involved in characterization are summarized next.

Density, ρ was measured using separate mass and volume measurements. Volume measurements for fluids were made using a 100 mL graduated cylinder. The mass measurements were conducted using an analytical balance by measuring the weight of the cylinder + liquids then subtracting the weight of the empty cylinder. Fluid viscosity, μ was measured using a Brookfield DV-II + PRO viscometer.

The interfacial tension, σ, was measured using a spinning drop tensiometer. The measurements were carried out in a capillary tube that contains the dense fluid, dyed water in this case. One drop of the less dense, nonwetting fluid, was placed in the dense fluid. The principle of measurement with a spinning-drop tensiometer is that rotating the horizontal tube creates a centrifugal force that elongates the liquid drop. The elongation stops when the centrifugal force and interfacial tension balances. Values obtained at this point are used to estimate surface tension as

$$\sigma = 0.25\Delta\rho\omega^2 r^3 \qquad (1)$$

where $\Delta\rho$ is the differences in density between two fluids, in kg/m^3, r is the radius of the drop in m, and the angular frequency, ω is defined as

$$\omega = \frac{2\pi}{f}1000 \qquad (2)$$

and f is the velocity recorded from the tensiometer, in msec/shaft revolution.

Micromodel experiment

Upon the completion of micromodel fabrication, fluid preparation, and characterization, a new micromodel was flushed with CO_2 for approximately 30 minutes under constant pressure in order to displace the air in the system. Then, the micromodel was flooded with distilled water until reaching breakthrough. Because CO_2 is very soluble in water, this step allows the micromodels to be fully saturated with water upon waterflooding. A drainage experiment is performed by injecting dyed water as the wetting phase into the water-saturated micromodel. After the micromodel is fully saturated with the dyed water, non-wetting phase is injected to displace the wetting phase under constant volumetric rate. For microscopic images, the visual section of the micromodel is divided into 9 squares, shown in Fig.5. At each time step, 9 microscopic images are taken along with macroscopic image showing the overall flow pattern.
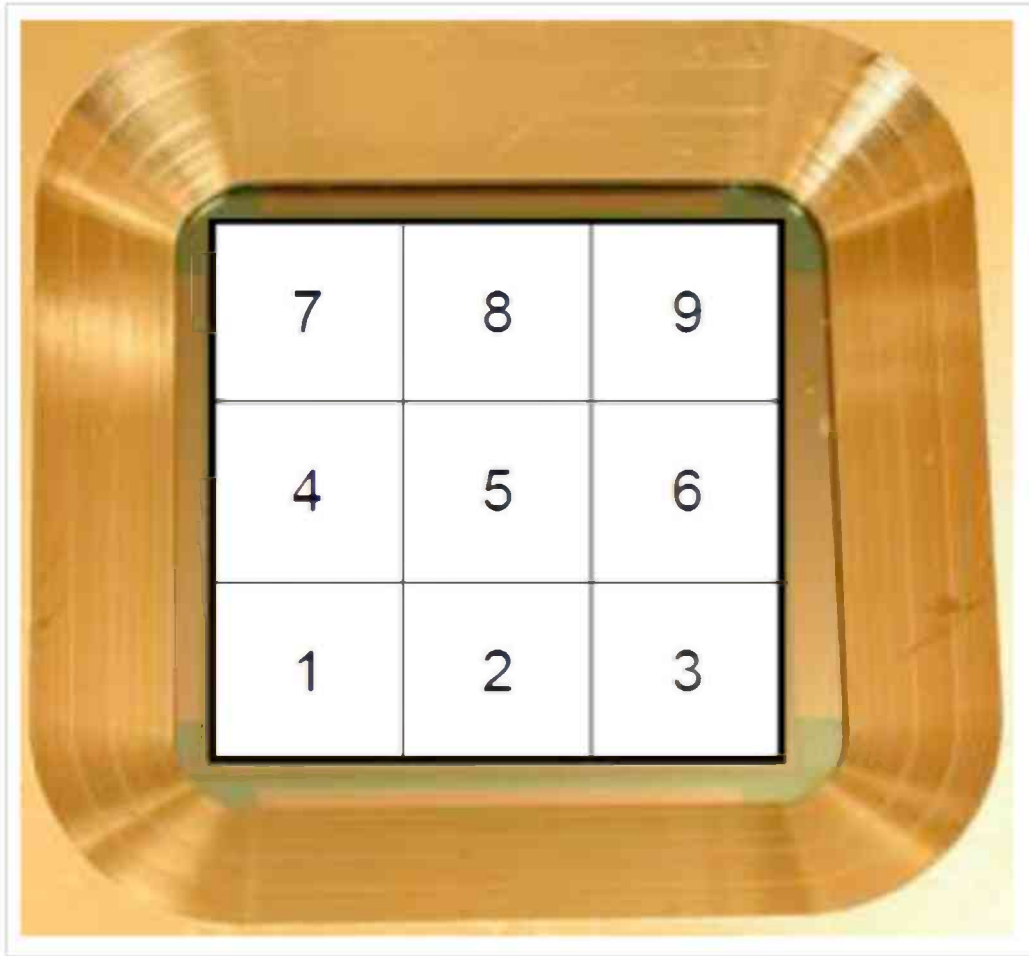
Figure 5: Division of micromodel for image capture.

Matlab image analysis tools were previously developed to quantify the wetting and non-wetting phase saturation (4). For experiments conducted with the brilliant green dye, it was difficult for Matlab image analysis to distinguish the contrast between the green-dyed wetting phase and clear non-wetting phase. Therefore GIMP, GNU Image Manipulation Program, was utilized to edit and quantify the phase saturation within images. The dyed wetting phase was manually colored in GIMP and therefore achieved a much greater contrast. This manual processing allowed the differentiation between two phases. For experiments conducted with the UV dye, phase constrast was much better. No preprocessing of images was necessary.

In both cases, the quantification of the image starts with the conversion of the Red Green Blue (RGB) images to binary (black and white) images. The threshold tool reduces the images to a binary black and white image. The histogram counts the percentage of black pixels of the image, therefore giving us the wetting phase saturation. In addition, the black section of the image sometimes includes the edge of the grains and edged surface of the micromodel because they have the same RGB value as the wetting phase. Hence, the extra edge effect has to be subtracted from the resulting black section percentage. The micromodel has an edge effect of 32.64% when viewed without the UV dye (1). The new percentage from the black section is divided by the porosity to calculate wetting and nonwetting phase saturation as

$$S_w = \frac{Black - EdgeEffect}{\phi} \qquad (3)$$

$$S_{nw} = 1 - S_w \qquad (4)$$

Experimental Results

Results from the various experiments are discussed in this section. A considerable number of experiments were conducted with addition of green dye to the aqueous phase as an image contrast agent. The detailed experimental conditions of these experiments including the fluid characterization are summarized in Table 2. Experiments were performed with different flow rates and viscosity ratios. The first experiment was designed to be the control set, where the viscosity ratio is less than 1 and under no gravity forces, which is favorable for stable displacement. In order to study the effect of gravity forces or Bond number, two experiments (Exps. 2-3) were conducted in a vertical setup. Experiment 4 was performed with unfavorable viscosity ratio in the horizontal displacement direction. Hence, the injection was carried out in either upward or downward direction. Experiment 5 decreased the capillary number by slowing down the injection rate. Finally experiment 6 further increased the viscosity ratio between the two phases to achieve even greater mobility ratio.

Representative results from monitoring the overall displacement pattern in the micromodel are shown in Fig. 6. This figure is a series of photographs of the entire micromodel at various times during a viscously unstable drainage (experiment 4 in Table 2). An unstable drainage is apparent as the undyed nonwetting phase displaces the defending green-dyed wetting phase. Note, however, the very low contrast between phases. Similar results obtained at greater magnification are shown in Fig 7.

13

Table 2: Description of experimental parameters. Subscripts "i" and "d" refer to injected and displaced fluids, respectively. Arrows indicate the direction of injection with respect to gravity.

	μ_i (cP)	μ_d (cP)	ρ_i (g/cm^3)	ρ_d (g/cm^3)	Q (ft/day)	M	IFT (dyne/cm)	Ca	Bo
1	3.22	1.06	0.76	0.97	37.8	0.33	17.2	2.50 x10^{-5}	7.48 x10^{-5}
2	3.22	1.06	0.76	0.97	37.8	0.33	17.2	2.50 x10^{-5}	-7.48 x10^{-5}
3	3.22	1.06	0.76	0.97	37.8	0.33	17.2	2.50 x10^{-5}	7.48 x10^{-5}
4	0.42	4.96	0.67	1.09	37.8	11.81	44.5	1.26 x10^{-6}	5.80 x10^{-5}
5	0.42	4.96	0.67	1.09	3.78	11.81	44.5	1.26 x10^{-7}	5.80 x10^{-5}
6	0.48	12.8	0.71	1.2	37.8	26.67	75.1	8.52 x10^{-7}	3.96 x10^{-5}

Displacement at the pore level is relatively poor and although the leading edge passes a particular region of pore space, drainage continues to occur in a progressive fashion. Figure 7 illustrates the drainage displacement front moving through a set of pores. The pores filled with wetting phase are greenish-blue due to the dye. The nonwetting phase is unshaded. Note the gradual decrease in the number of pores that are dyed. This image also well illustrates the difficulty that we faced in quantifying our experimental data using the green dye in the aqueous phase. Image quality makes it difficult to discern rapidly the presence and distribution of the advancing nonwetting phase.

The thesis of Gu (14) contains results from the full set of experiments conducted with green dye in the wetting phase. While the matched viscosity ratio experiments (Table 2) gave repeatable results, the contrast between wetting and nonwetting phase was quite unsatisfying and led to significant noise during the analysis. Application of image analysis techniques to pore-level and whole micromodel images was shown to be feasible, but overly laborious given the volume of images to be processed. It was decided to pursue a different means of obtaining phase contrast and to use the generally successful experimental protocols established. Accordingly, the brilliant green dye in the aqueous phase was replaced with a dye that fluoresces when exposed to UV light.

A new and expanded set of experiments was then run. These experiments are discussed in detail next. Figure 8 and Table 3 provide an overview of the viscosity ratio, M, and capillary number, Ca, of each experiment conducted. Each symbol on the figure represents an experiment. We span three orders of magnitude of Ca and four orders of magnitude in M.

Drainage results – whole micromodel images

With the addition of a UV-sensitive dye to the aqueous phase, the microscope is illuminated with a black light in the form of a UV ring. The frequency of the UV light is 340 nm. The UV dye fluoresces and the wetting phase appears greenish in tint to the naked eye as well as in photographs and microscope images as illustrated in Fig. 9. The injected nonwetting phase is black. The purple ring-like artifact near
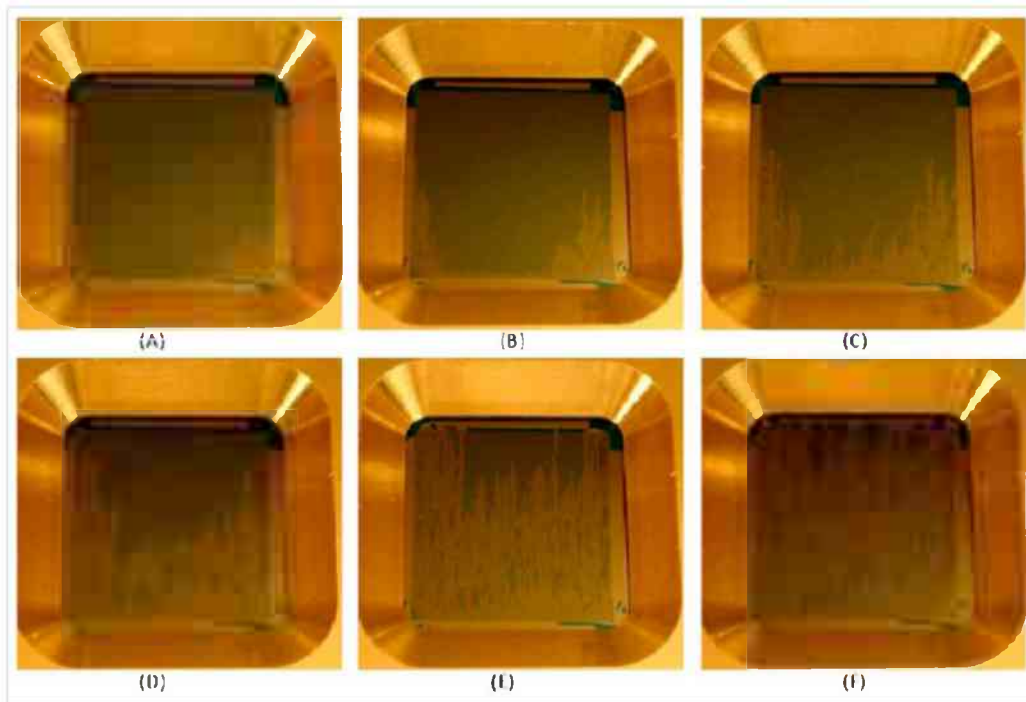
Figure 6: Experiment 4 with green dye. Viscously unstable displacement at a mobility ratio of 11.81. (A) 0.25 PV injected/fully saturated with wetting phase (B) 0.41 PV injected (C) 0.54 PV injected (D) 0.71 PV injected (E) 0.83 PV injected and (F) 0.95 PV injected.
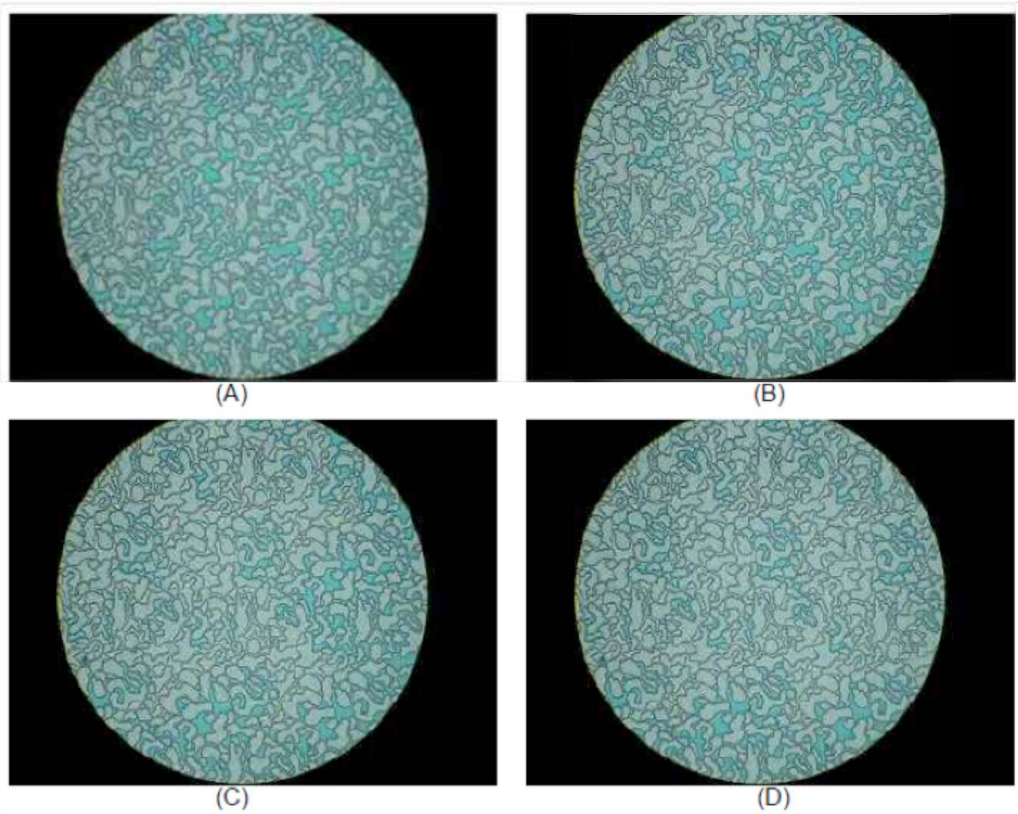
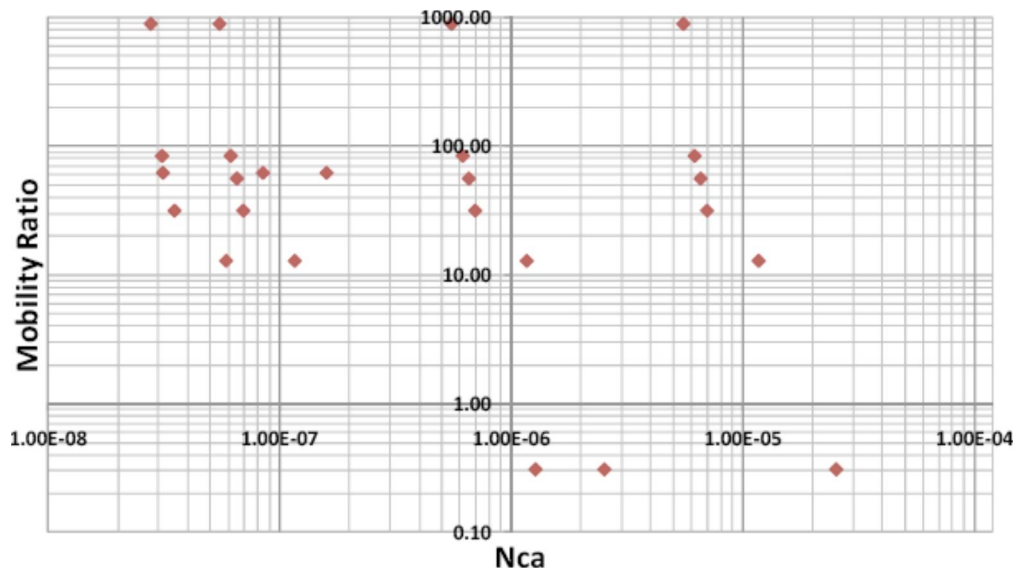Figure 7: Experiment 6. Pore-scale images (A) to (D) increasing time.

Figure 8: Overview of the parameters defining drainage displacement experiments.

Table 3: Overview of experiments conducted with UV-sensitive dye in the water phase. Subscripts "i" and "d" refer to injected and displaced fluids, respectively. All experiments are horizontal

Fluids	No.	μ_i (cP)	μ_d (cP)	ρ_i (g/cm^3)	ρ_d (g/cm^3)	Q (ft/day)	M	Ca
hexadecane-water	1	3.22	1.00	0.76	0.97	1.92	0.31	1.27 x10^{-6}
	2	3.22	1.00	0.76	0.97	3.80	0.31	2.51 x10^{-6}
	3	3.22	1.00	0.76	0.97	38.0	0.31	2.51 x10^{-5}
	4	3.22	1.00	0.76	0.97	380.	0.31	2.51 x10^{-4}
nheptane-50/50	5	0.39	5.00	0.67	1.13	1.92	13.0	5.87 x10^{-8}
glycerin/water	6	0.39	5.00	0.67	1.13	3.80	13.0	1.16 x10^{-7}
	7	0.39	5.00	0.67	1.13	38.0	13.0	1.16 x10^{-6}
	8	0.39	5.00	0.67	1.13	380.	13.0	1.16 x10^{-5}
nheptane-65/35	9	0.39	12.40	0.67	1.16	1.92	31.8	3.52 x10^{-8}
glycerin/water	10	0.39	12.40	0.67	1.16	3.80	31.8	6.96 x10^{-8}
	11	0.39	12.40	0.67	1.16	38.0	31.8	6.96 x10^{-7}
	12	0.39	12.40	0.67	1.16	380.	31.8	6.96 x10^{-6}
nheptane-75/25	13	0.39	22.00	0.67	1.19	3.80	56.4	6.54 x10^{-8}
glycerin/water	14	0.39	22.00	0.67	1.19	38.0	56.4	6.54 x10^{-7}
	15	0.39	22.00	0.67	1.19	380.	56.4	6.54 x10^{-6}
nheptane-80/20	16	0.39	33.00	0.67	1.20	1.92	84.6	3.11 x10^{-8}
glycerin/water	17	0.39	33.00	0.67	1.20	3.80	84.6	6.15 x10^{-8}
	18	0.39	33.00	0.67	1.20	38.0	84.6	6.15 x10^{-7}
	19	0.39	33.00	0.67	1.20	380.	84.6	6.15 x10^{-6}
nheptane-	20	0.39	350.0	0.67	1.26	1.92	897.4	2.78 x10^{-8}
99% glycerin	21	0.39	350.0	0.67	1.26	3.80	897.4	5.50 x10^{-8}
	22	0.39	350.0	0.67	1.26	38.0	897.4	5.50 x10^{-7}
	23	0.39	350.0	0.67	1.26	380.	897.4	5.50 x10^{-6}
CO$_2$-water	24	0.02	1.00	0.002	1.00	40.0	62.5	3.14 x10^{-8}
	25	0.02	1.00	0.002	1.00	108.0	62.5	8.47 x10^{-8}
	26	0.02	1.00	0.002	1.00	203.0	62.5	1.59 x10^{-7}

the edges of the image is a reflection of the UV light ring off of the class cover plate of the micromodel. The image is of the entire etched pattern of the micromodel. A significant question resulting from the switch to a UV-sensitive dye was the applicability of image analysis techniques on the results. The lower images in Fig. 9 result after standard image analysis techniques of segmentation and conversion to a binary image. Note that the shape of the drainage displacement front is maintained in its entirety and that the ring-like artifact, while still visible, has not contributed any significant problems to the conversion to a binary black and white image. Again, the injected nonwetting phase is black in the lower images.
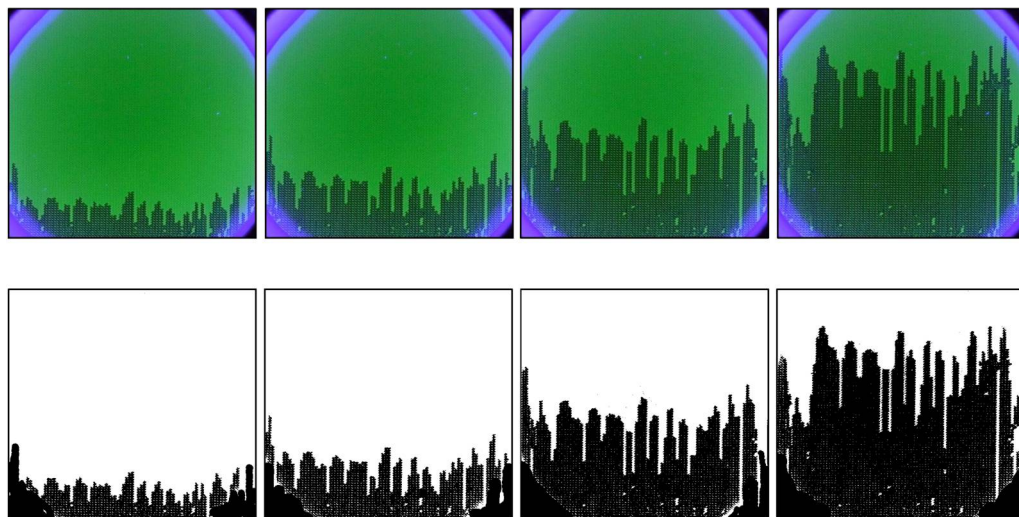
Figure 9: Typical drainage displacement results using a UV-sensitive dye in the wetting phase. Top: injected nonwetting phase is dark and the wetting phase has a greenish tint. Bottom: images have been segmented and converted to binary black and white. The displacement is for $Ca = 12.95$ and $M = 1.16 \times 10^{-6}$. From left to right, the elapsed time of each image is 00:15, 00:33, 01:03, and 01:55 (min:sec).

The initial tests were performed under favorable low viscosity ratio ($M < 1$) conditions at a variety of capillary numbers. These tests set the baseline with the simplest conditions of favorable density and viscosity to compare with more complex experiments. A more viscous fluid, hexadecane, was injected to displace distilled water. The viscosity ratio is ($M =$) 0.31 and Bo is 7.48×10^{-5}. The very small bond number indicates the experiment is carried under neutral buoyancy effect. Four baseline drainage displacements were conducted at Ca of $1.26 \times 10^{-6}, 2.51 \times 10^{-6}, 2.51 \times 10^{-5}$, and 2.51×10^{-4}. Figure 10 presents the displacement sequence at $Ca = 2.51^{-5}$. Because the drainage displacement has a favorable mobility ratio, frontal movement appears relatively smooth and stable. The front starts from the injection port on the bottom left and progresses through the micromodel. Small irregularities in the displacement front are apparent. Displacements at this mobility ratio but other capillary numbers appear to be similar. As expected, these tests present a stable drainage displacement control set.

A series of drainage displacements was then run at increasingly unfavorable condi-

tions. We present images of the time evolution of the displacement at a particular M and for a variety of Ca. As the velocity of the displacement increases, and accordingly the Ca increases, we expect the drainage displacement pattern to change somewhat. Generally, we examine four distinct Ca for each M. This makes for a presentation with a very large number of figures, but does document well the experimental results obtained. All of the Ca examined are within the parameter range expected for CO_2 sequestration.
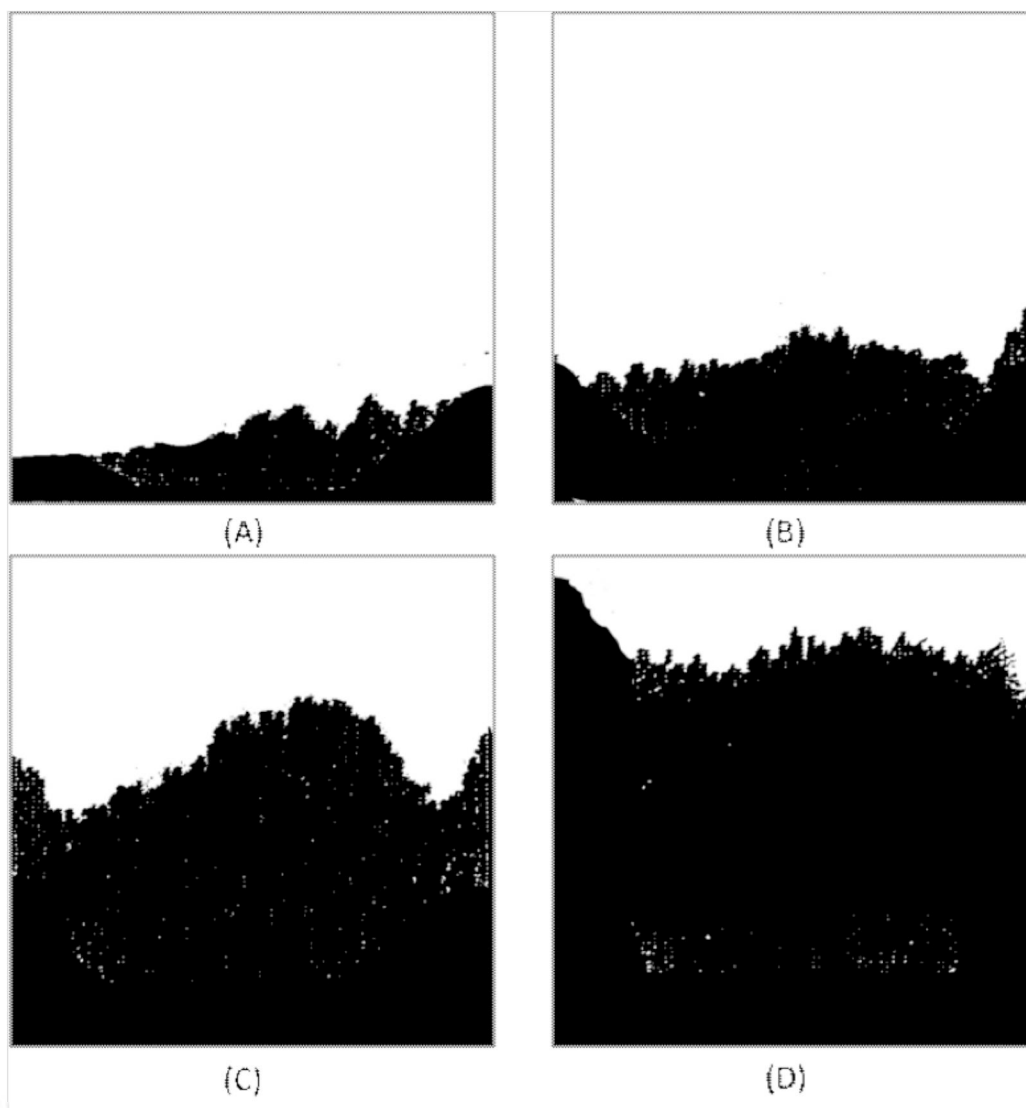
Figure 10: Typical stable drainage displacement results at $M = 0.31$ and $Ca = 2.51 \times 10^{-5}$. (A) 00:50 (min:sec) , (B) 2:30, (C) 5:40, (D) 10:00.

The second set of tests was conducted with a mixture of 50 wt% water and glycerin as the wetting phase and n-heptane as the nonwetting phase. The M was equal to 12.95. Displacements were conducted at $Ca = 5.87 \times 10^{-8}, 1.16 \times 10^{-7}, 1.16 \times 10^{-6}$,
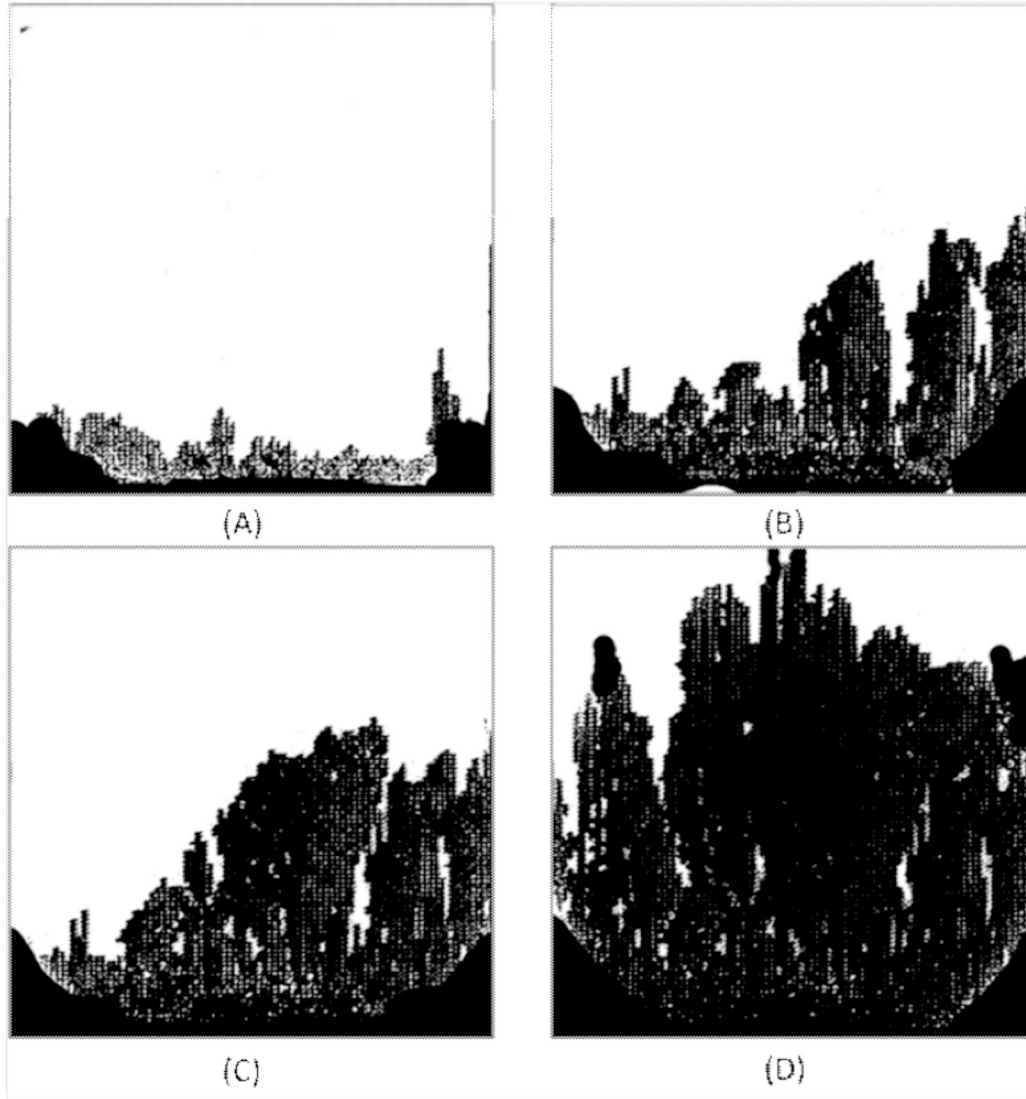
and 1.16×10^{-5}. Figures 11 to 14 present snap shots of the results at various times. In contrast to the stable drainage displacement (Fig. 10), the displacement front is quite irregular. At the smallest $Ca = 5.87 \times 10^{-8}$, a relatively large and broad finger forms in the rightmost portion of the micromodel. As the Ca and frontal displacement speed increase, the front becomes less organized and greater number of thin fingers are apparent. It is interesting that fingers are relatively short and thin throughout these tests even though the mobility ratio is quite unfavorable.
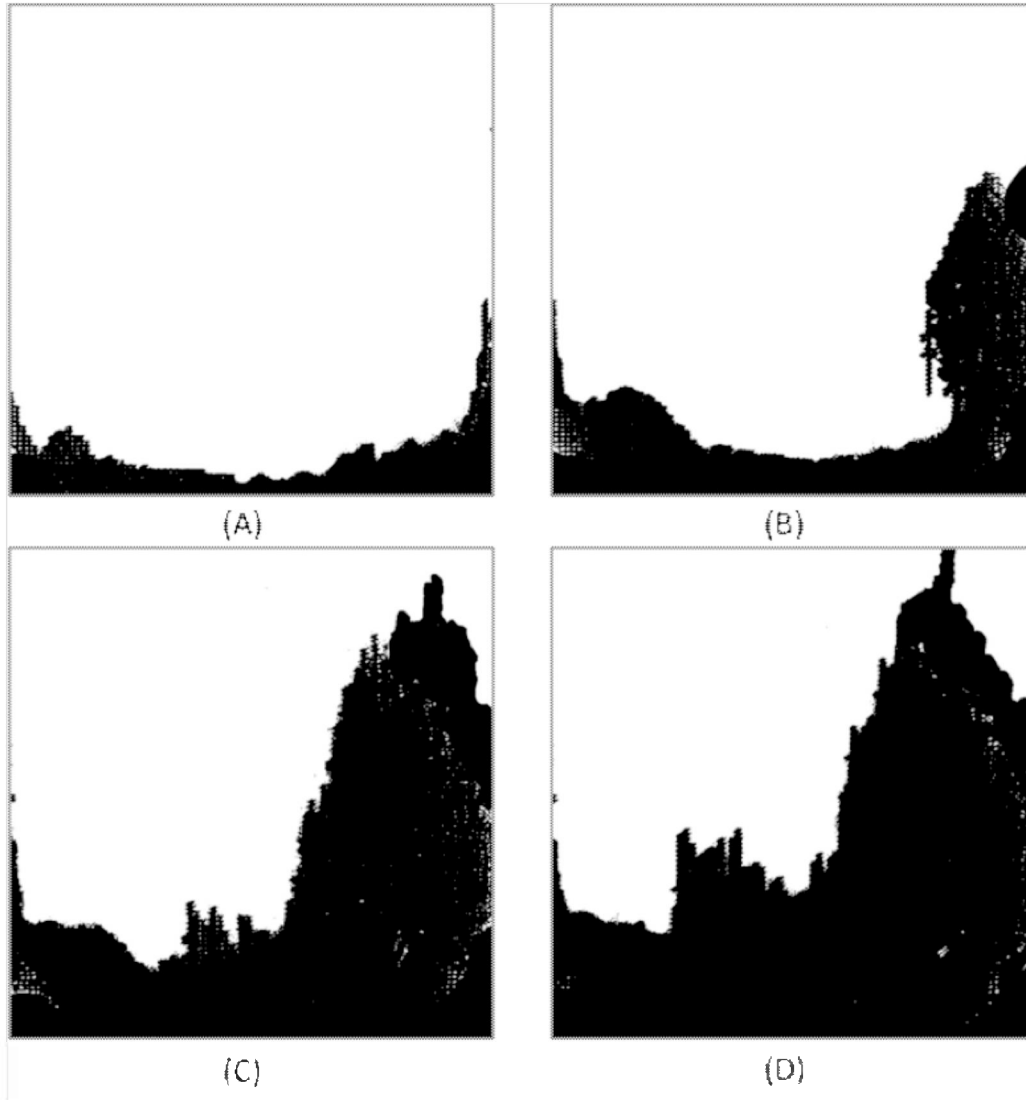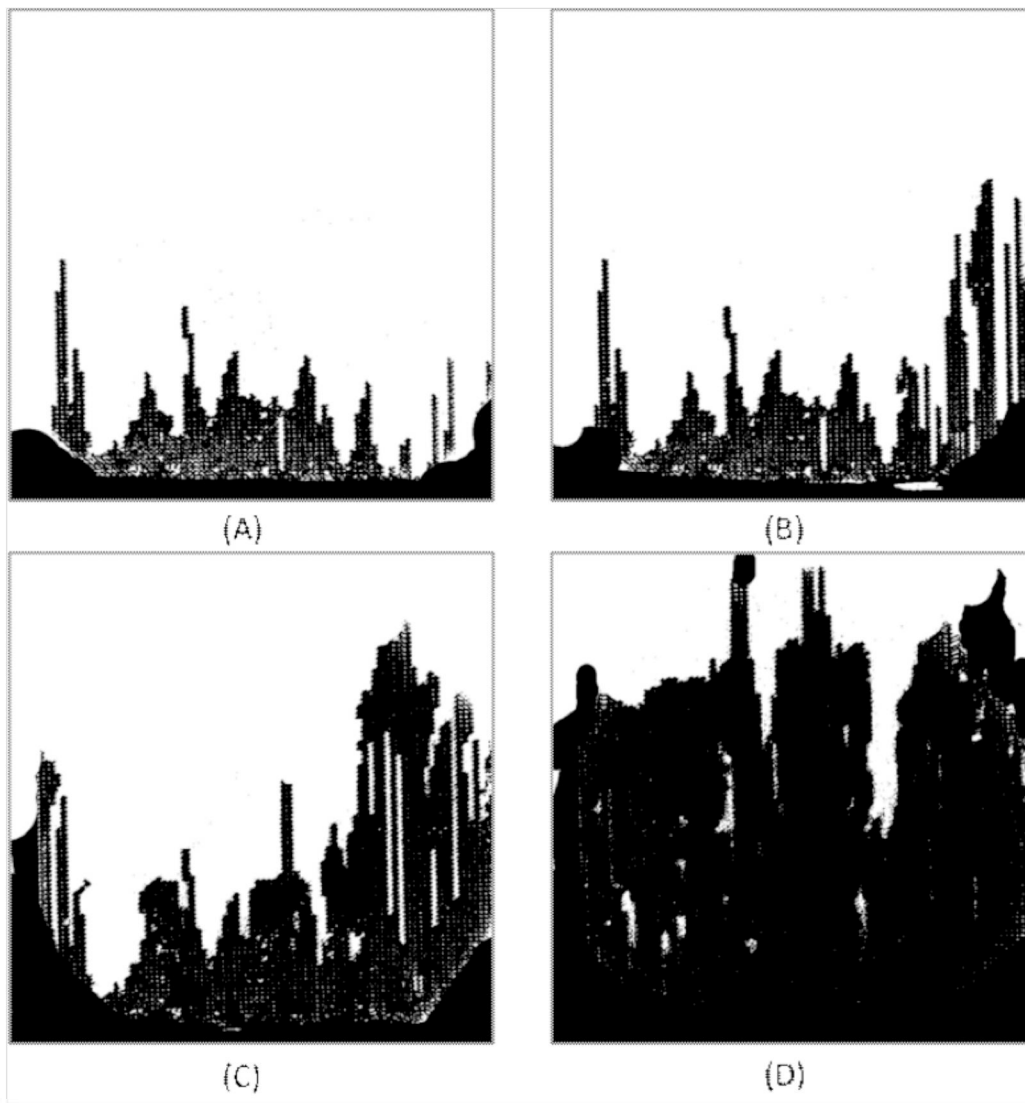

Figure 11: Drainage displacement results at $M = 12.95$ and $Ca = 5.87 \times 10^{-8}$. (A) 16:16 (min:sec), (B) 49:10, (C) 57:15, (D) 81:20.

The third set of tests was conducted with a mixture of 65 wt% glycerin and 35 wt% water as the wetting phase and n-heptane as the nonwetting phase. The M was equal to 31.79. Displacements were conducted at $Ca = 3.52 \times 10^{-8}$, 6.96×10^{-8}, 6.96×10^{-7},

Figure 12: Drainage displacement results at $M = 12.95$ and $Ca = 1.16 \times 10^{-7}$. (A) 00:30 (min:sec), (B) 5:25, (C) 8:30, (D) 17:45.
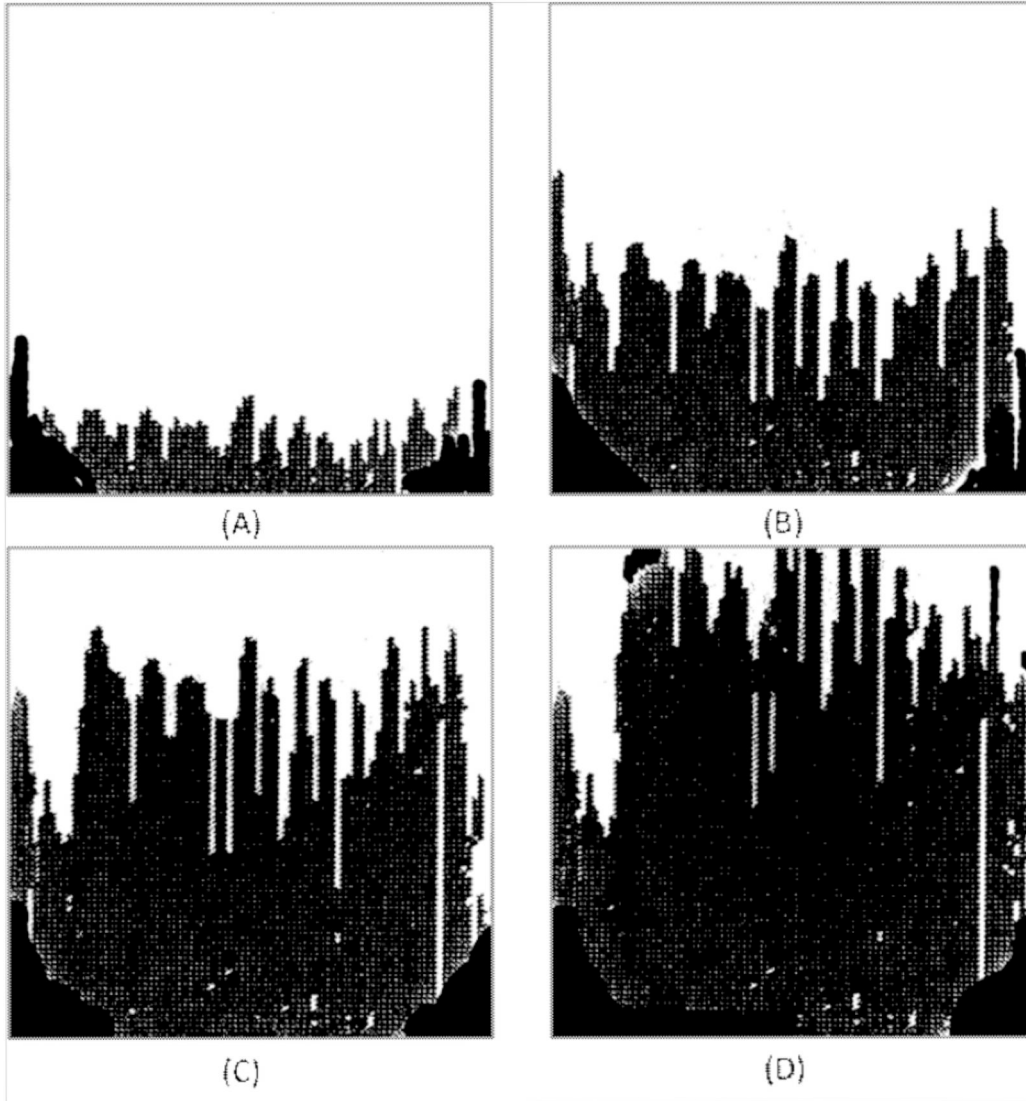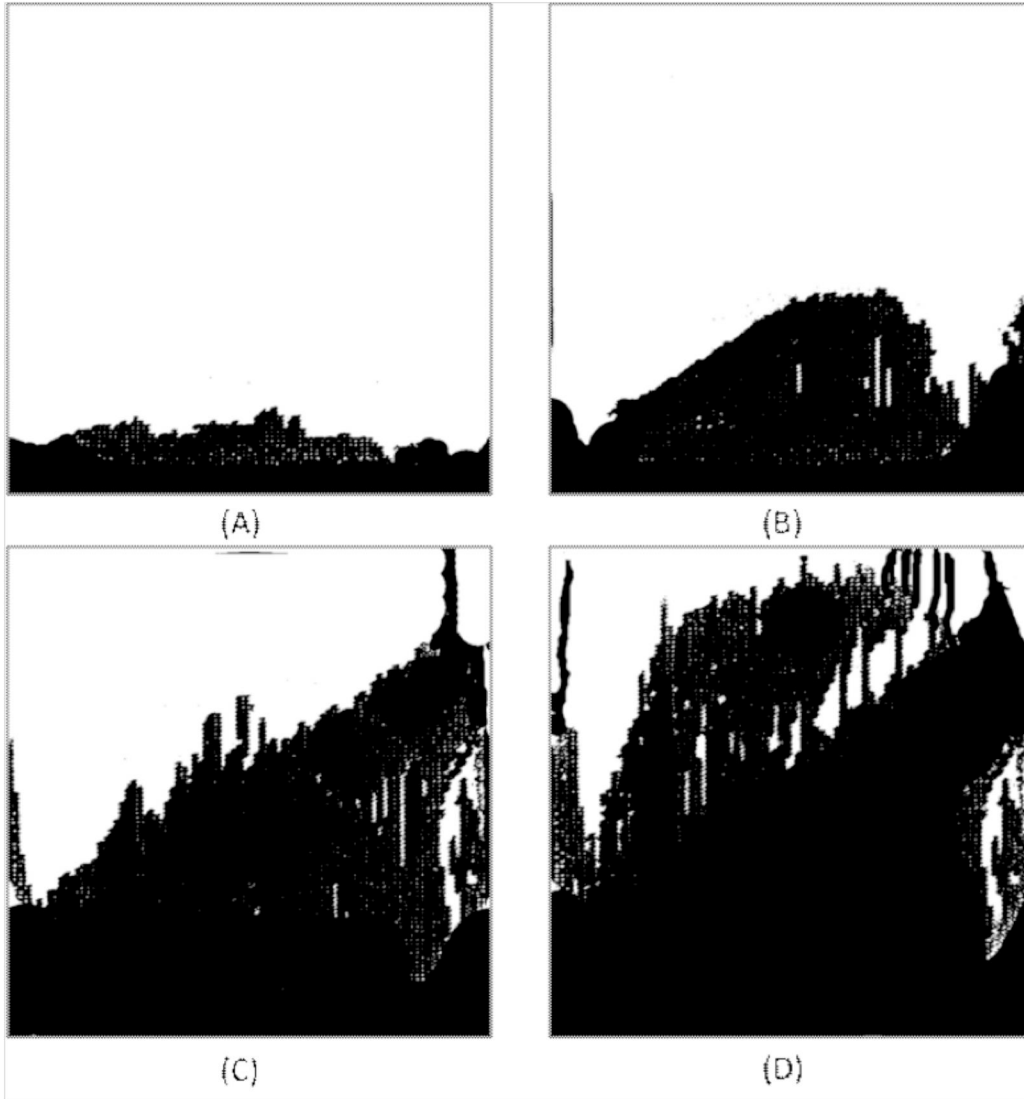
Figure 13: Drainage displacement results at $M = 12.95$ and $Ca = 1.16 \times 10^{-6}$. (A) 00:15 (min:sec), (B) 1:03, (C) 1:15, (D) 1:55.
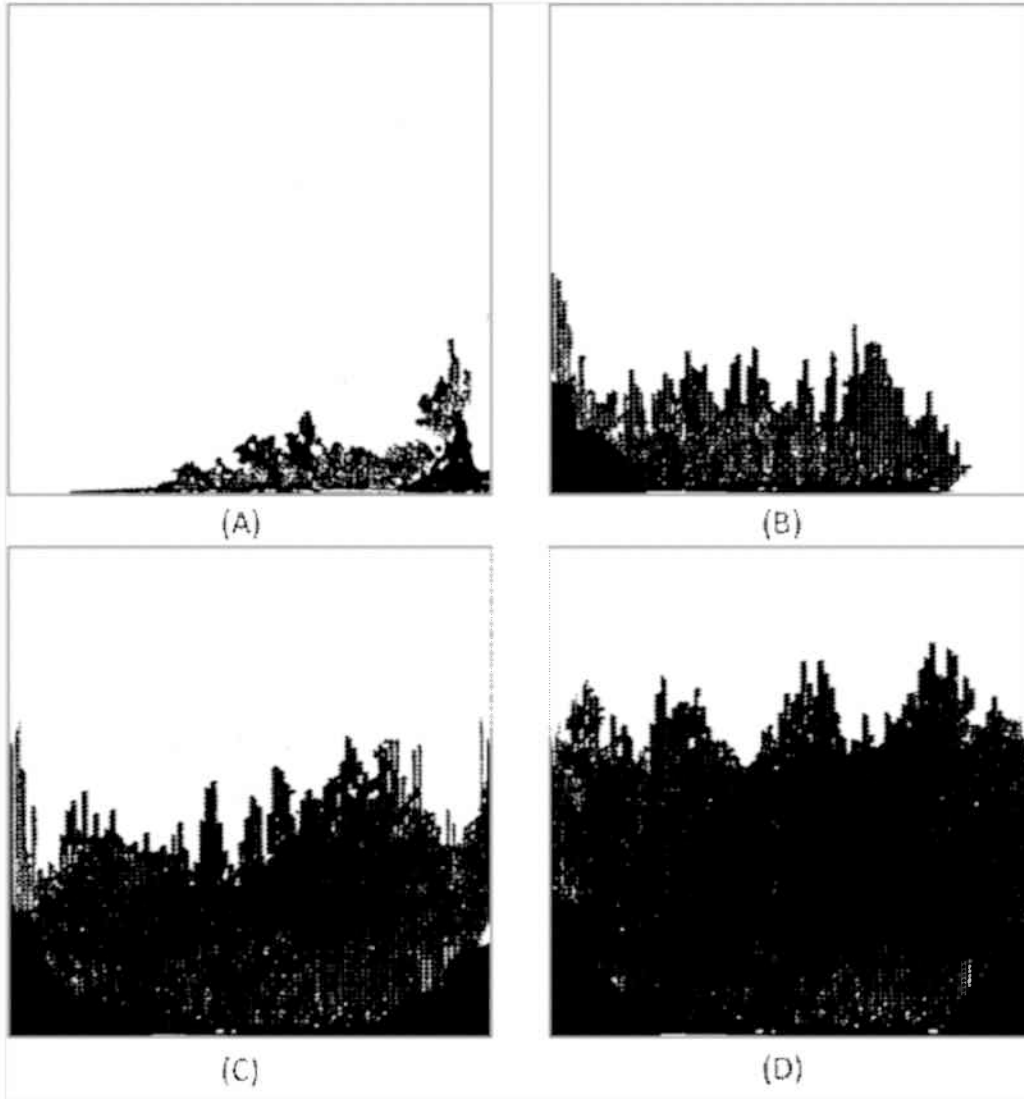
Figure 14: Drainage displacement results at $M = 12.95$ and $Ca = 1.16 \times 10^{-5}$. (A) 00:05 (min:sec), (B) 00:15, (C) 00:22, (D) 00:50.

and 6.96×10^{-6}. Figures 15 to 18 present snap shots of the results at various times. In contrast to the stable drainage displacement (Fig. 10), the displacement front is irregular at any injection rate (ie Ca). The fingers appear to be longer and thinner compared to the displacements at $M = 12.95$.

Figure 15: Drainage displacement results at $M = 31.79$ and $Ca = 3.52 \times 10^{-8}$. (A) 1:40 (min:sec), (B) 4:15, (C) 13:20, (D) 32:00.

The fourth set of tests was conducted with a mixture of 75 wt% glycerin and 25 wt% water as the wetting phase and n-heptane as the nonwetting phase. The M was equal to 56.1. Displacements were conducted at $Ca = 6.54 \times 10^{-8}, 6.54 \times 10^{-7}$, and 6.54×10^{-6}. Figures 19 to 21 present snap shots of the results at various times. Nominally, these are the most unstable displacements witnessed thus far. Unstable structures are clearly visible and dominate the displacement. Interestingly,

24

Figure 16: Drainage displacement results at $M = 31.79$ and $Ca = 6.96 \times 10^{-8}$. (A) 1:40 (min:sec), (B) 7:10, (C) 13:10, (D) 21:10.
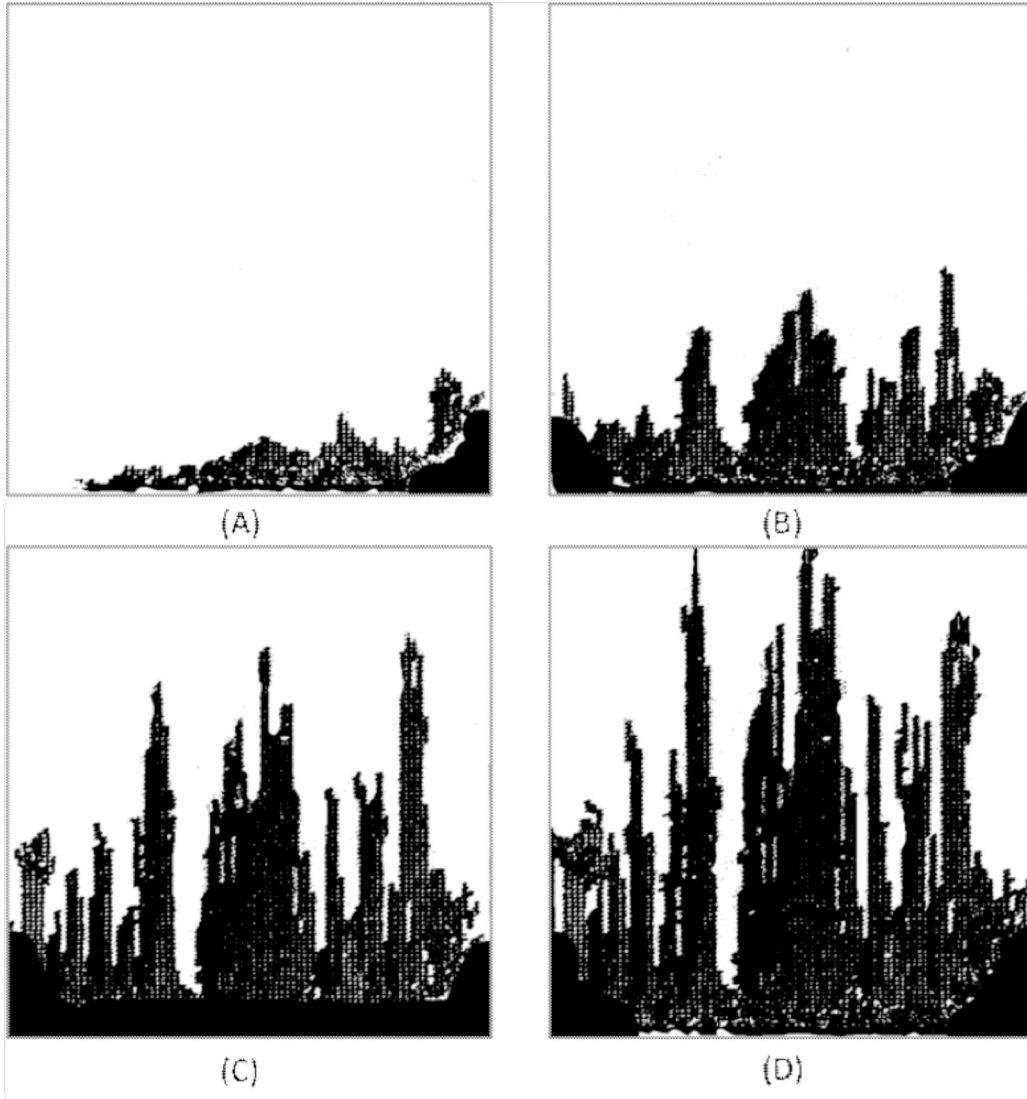
Figure 17: Drainage displacement results at $M = 31.79$ and $Ca = 6.96 \times 10^{-7}$. (A) 00:20, (B) 00:55, (C) 1:22, (D) 2:12.
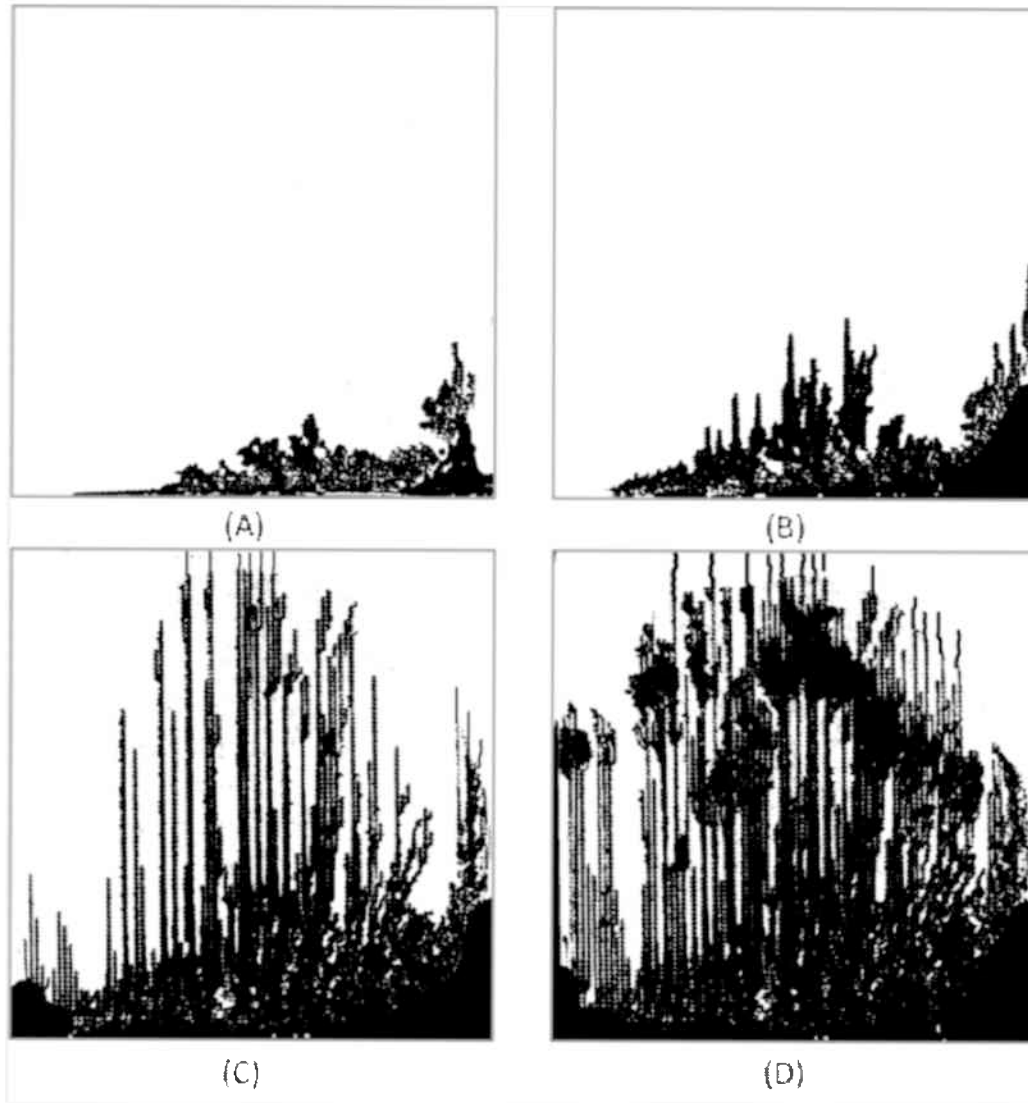
Figure 18: Drainage displacement results at $M = 31.79$ and $Ca = 6.96 \times 10^{-6}$. (A) 00:11 (min:sec), (B) 00:20, (C) 00:31, (D) 00:42.

multiple fingers are present and the displacements have surprising order for such a large viscosity contrast. Although not shown, we comment that each displacement in this test was conducted in duplicate to verify the results.
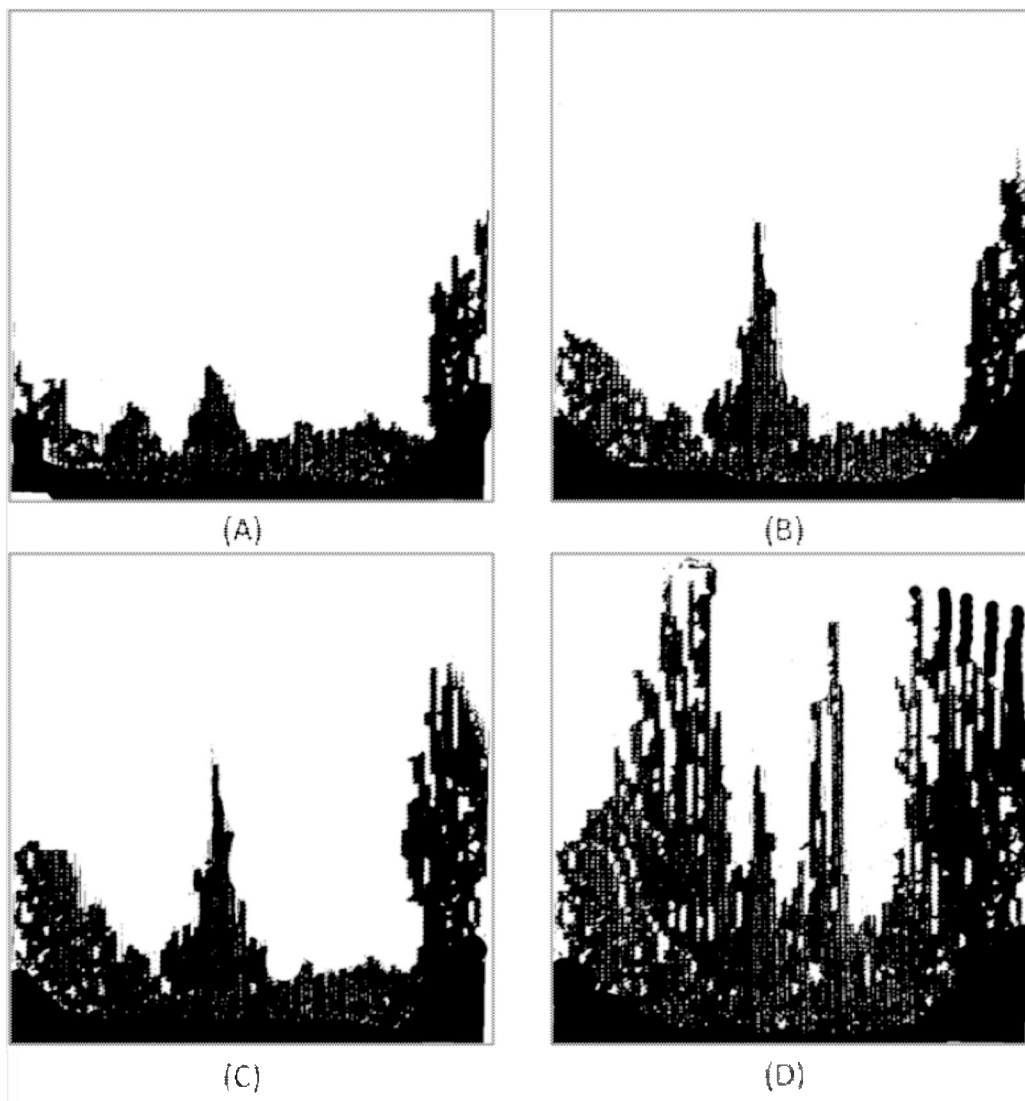

Figure 19: Drainage displacement results at $M = 56.1$ and $Ca = 6.54 \times 10^{-8}$. (A) 00:20 (min:sec), (B) 6:00, (C) 11:00, (D) 19:00.

The fifth set of tests was conducted with a mixture of 80 wt% glycerin and 20 wt% water as the wetting phase and n-heptane as the nonwetting phase. The M was equal to 84.6 representing, presumably, a quite unstable flood. Displacements were conducted at $Ca = 3.11 \times 10^{-8}, 6.15 \times 10^{-8}, 6.15 \times 10^{-7}$, and 6.15×10^{-6}. Figures 22 to 25 present snap shots of the results at various times for each Ca. Nominally, these are the most unstable displacements witnessed thus far. Unstable displacement structures quite similar to the previous results at $M = 56.1$ are clearly visible. Multiple fingers
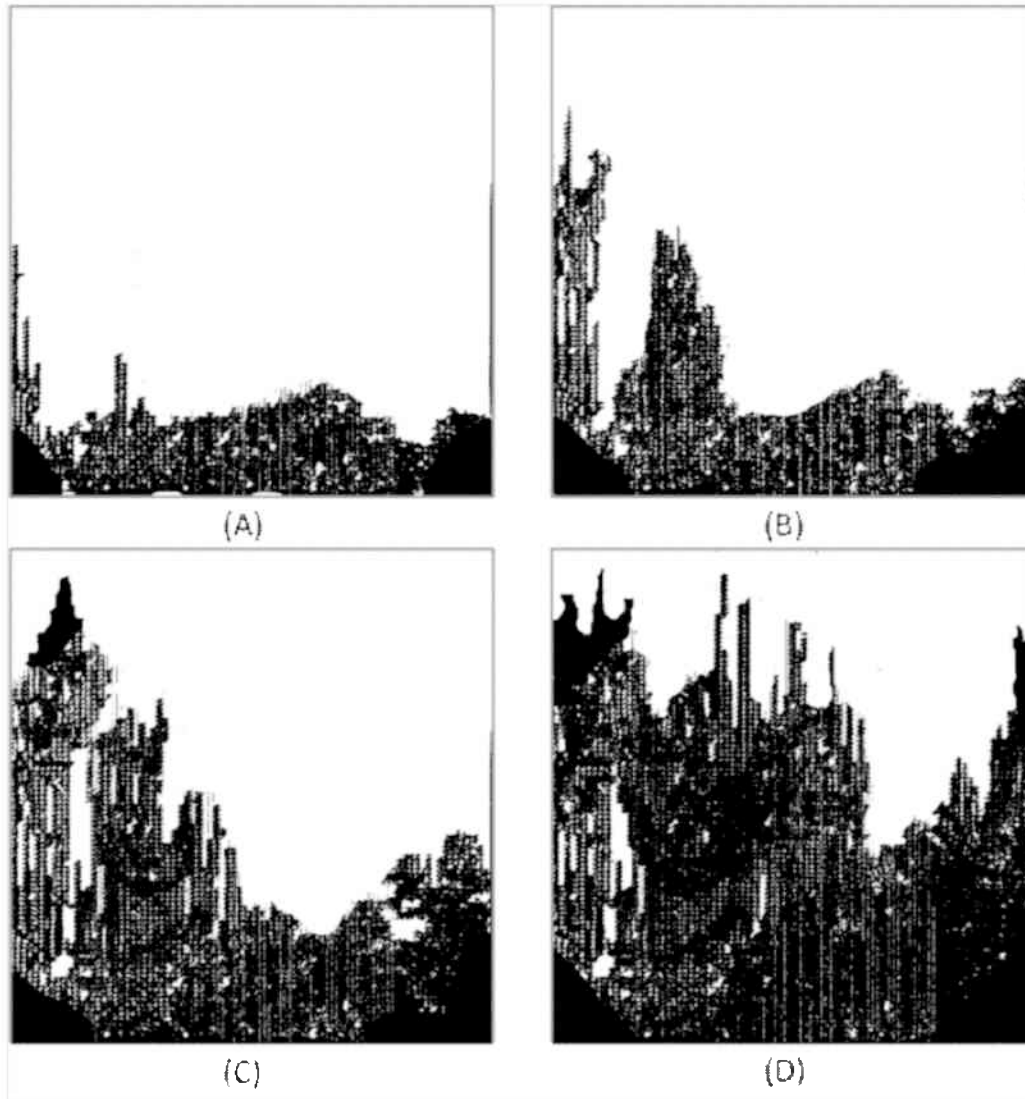
Figure 20: Drainage displacement results at $M = 56.1$ and $Ca = 6.54 \times 10^{-7}$. (A) 00:50 (min:sec), (B) 1:30, (C) 2:35, (D) 6:00.
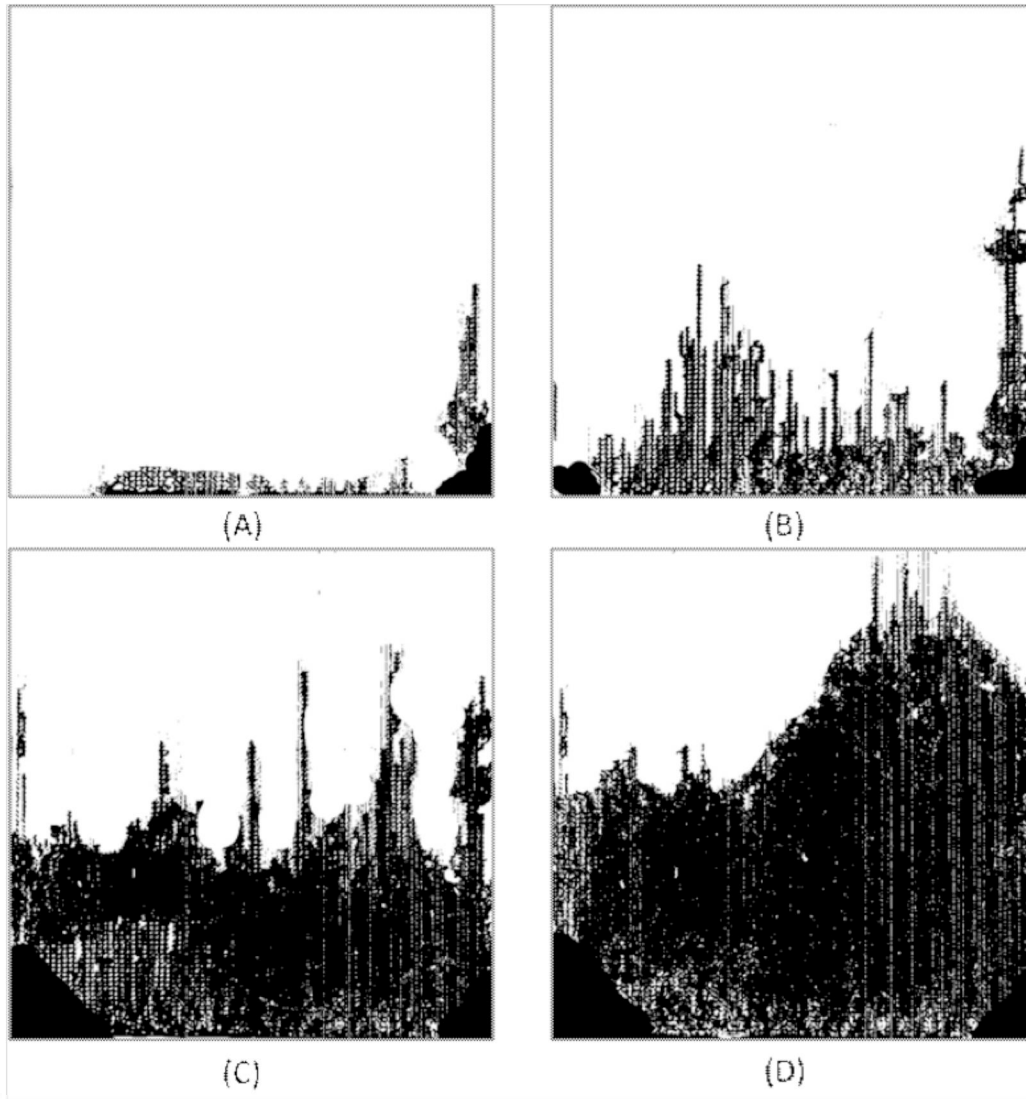
Figure 21: Drainage displacement results at $M = 56.1$ and $Ca = 6.54 \times 10^{-6}$. (A) 00:11 (min:sec), (B) 00:25, (C) 00:50, (D) 1:12.

initiate and propagate. As time progress, significant wetting phase is behind the leading edges of the displacement. Refer to images at later times, frames (C) and (D) in Figs. 22 to 25. These results indicate that while the areal sweep of the micromodel by the nonwetting phase is reasonably good for such a high mobility ratio, the local displacement efficiency is not high and significant fractions of the pore space, at the microscopic level, are not filled with nonwetting phase. This comment applies to a large fraction of the images obtained for drainage at M greater than 10.
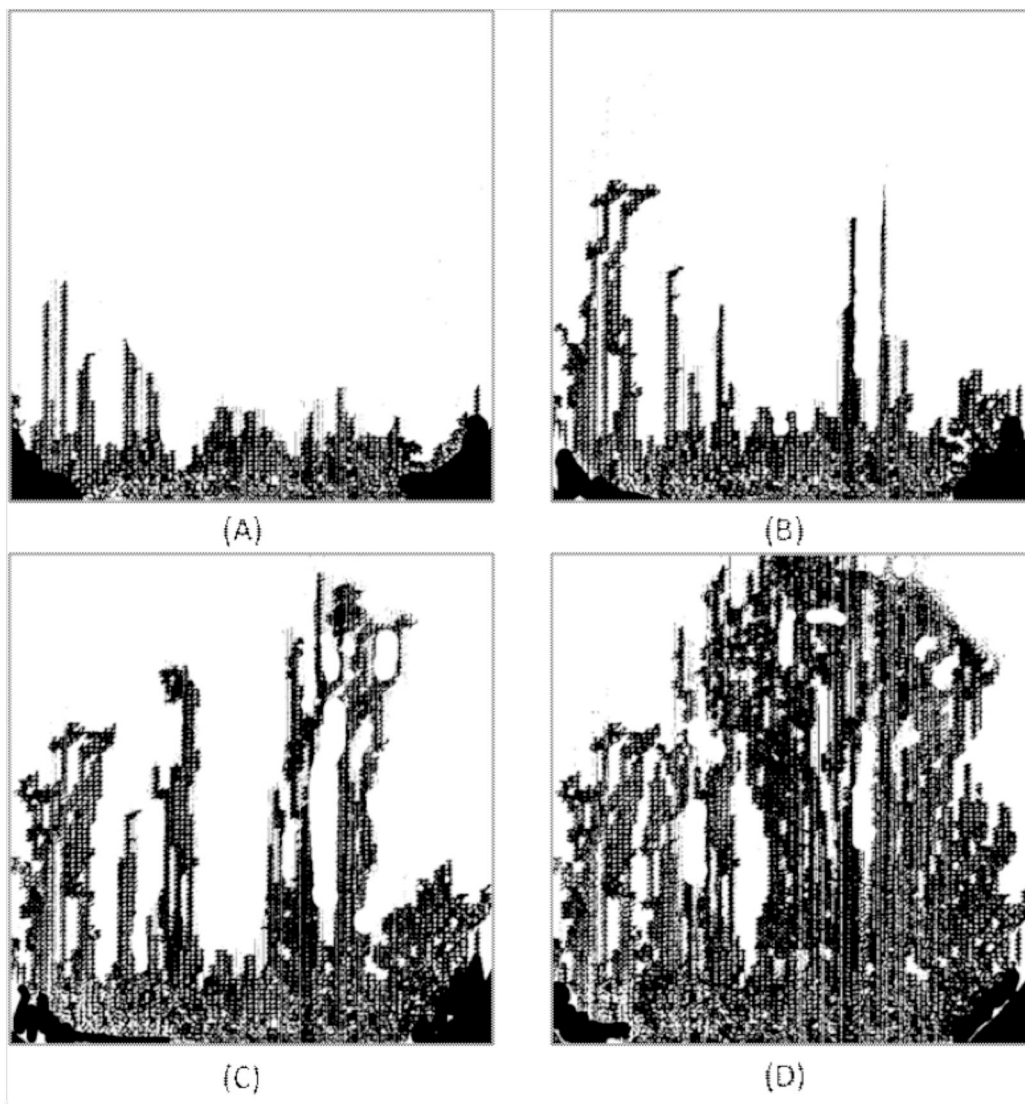

Figure 22: Drainage displacement results at $M = 84.62$ and $Ca = 3.11 \times 10^{-8}$. (A) 2:10 (min:sec), (B) 2:50, (C) 4:40, (D) 12:30.

As presented, a series of experiments that spanned mobility ratios from, essentially, 0.3 to 900 were conducted using matched viscosity ratio, preequilibrated fluids. The range of displacement patterns witnessed was remarkable and we have sought
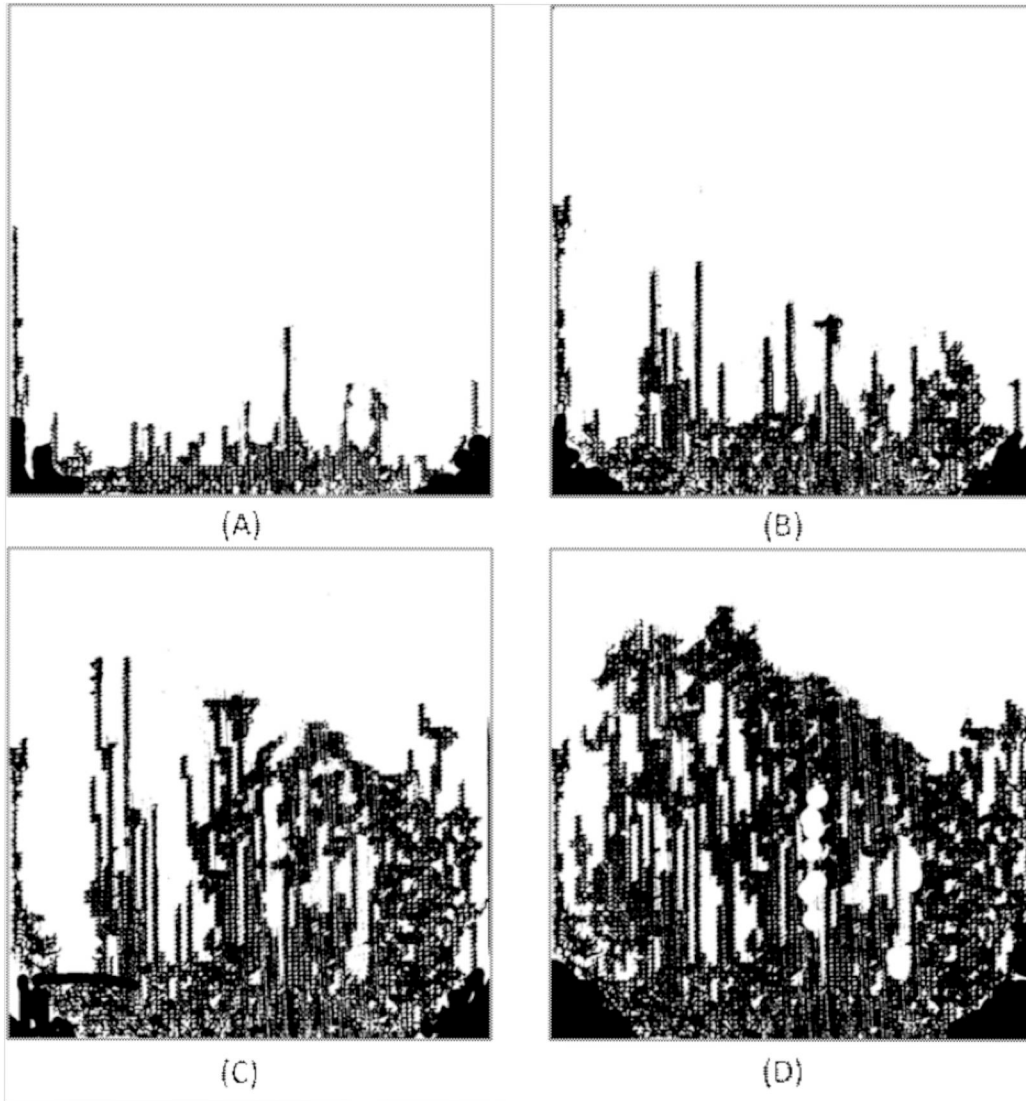
Figure 23: Drainage displacement results at $M = 84.62$ and $Ca = 6.15 \times 10^{-8}$. (A) 1:00 (min:sec), (B) 1:15, (C) 5:10, (D) 13:30.
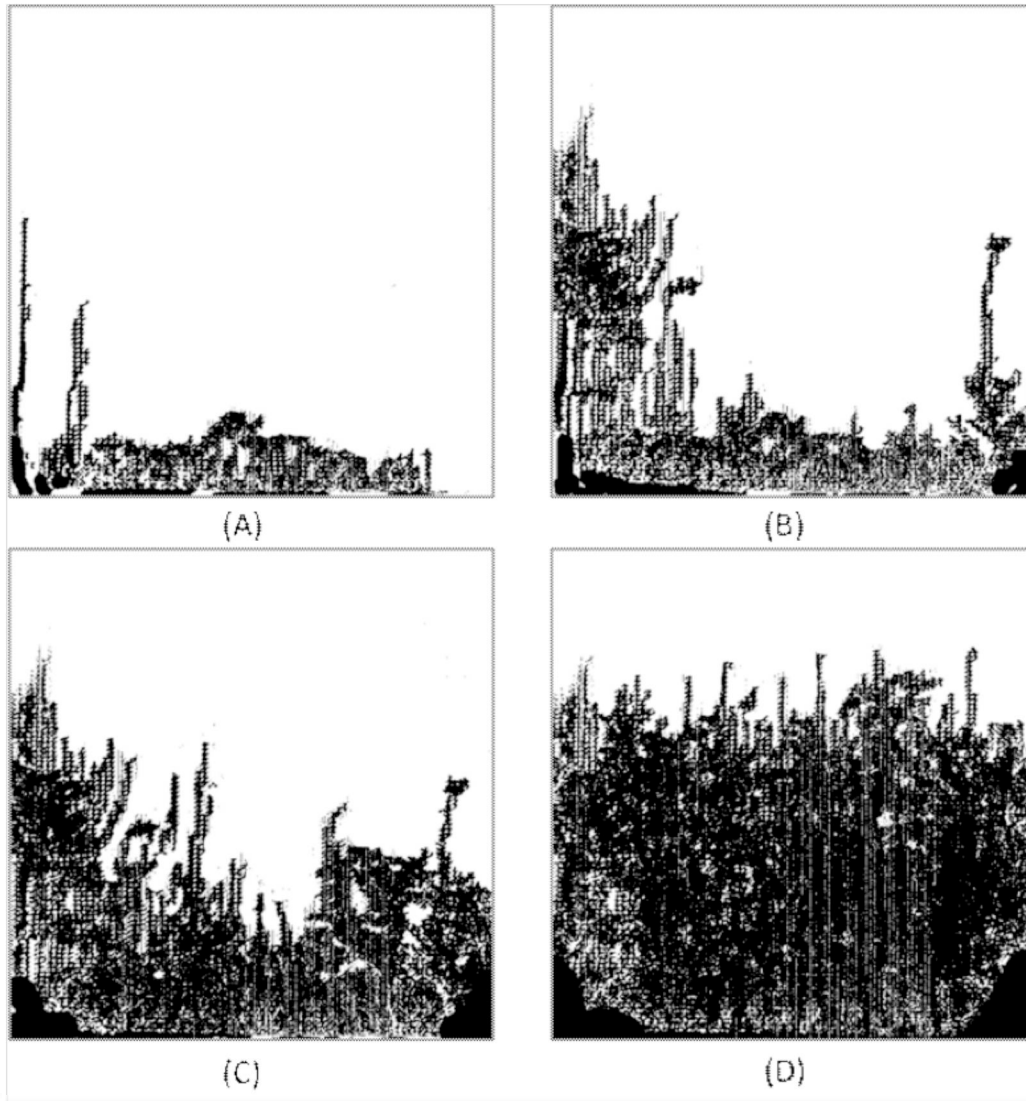
Figure 24: Drainage displacement results at $M = 84.62$ and $Ca = 6.15 \times 10^{-7}$. (A) 00:40 (min:sec), (B) 1:43, (C) 5:15, (D) 7:30.
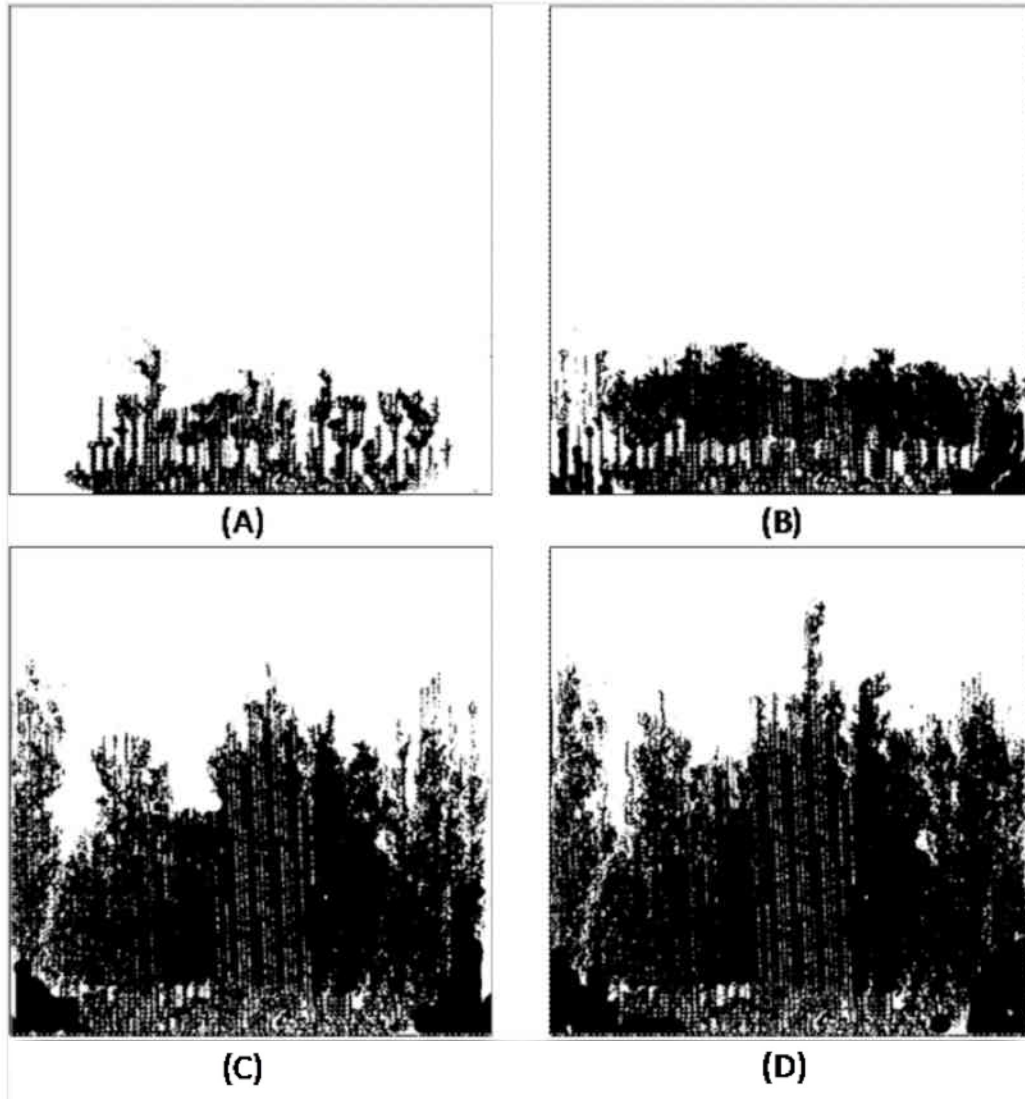
Figure 25: Drainage displacement results at $M = 84.62$ and $Ca = 6.15 \times 10^{-6}$. (A) 00:10 (min:sec), (B) 00:25, (C) 00:40, (D) 00:55.

to condense results for easier comparison and discussion. Figure 26 is a result of this effort. The figure plots M versus Ca and shows characteristic distributions of invading and draining phases as the parameter space is varied. The nonwetting phase is darkly shaded and the wetting phase is white, or lightly shaded. Each image on the plot is a snapshot of the phase distribution in the entire micromodel. For M of about 1 and less, displacement fronts are quite orderly and stable. There are no extensive fingers or irregularities in the front. Unstable displacement fronts are found for all displacements with M above 10. Fingers emerge at very early time scales and propagate through the micromodel. Nonwetting fluid continues to fill pore space well behind the leading edge of the displacement front in many of these cases. The Ca appears to play a small role in the macroscopic behavior in that fingers merge more readily at the greater flow rates.

An interesting feature at this scale and in these particular porous media, is the relatively benign aspect of the instabilities in comparison to miscible viscous instabilities. Multiple fingers form and lead the displacement followed by a relatively well organized transition from brine-filled to two-phase occupied pores. Recall that displacements are completely immiscible as fluids are preequilibrated to reduce any dissolution effects. The relatively smooth transition in unstable displacement behavior as Ca and M are modified, suggests that the phenomena found should ultimately be predictable from first principles.

Figure 27 is the view in an ensemble of pores after the nonwetting phase has entered and sufficient time has been allowed to drain the wetting phase to an irreducible saturation. The nonwetting phase and the grains are darkly shaded and the wetting phase is white, or lightly shaded. At the microscopic scale, the nonwetting phase has invaded the pore space and effectively drained the wetting phase. At low displacement rates (Ca), the connate, or remaining, water saturation is distributed in smaller "pockets" as compared to the larger Ca displacement. We do not refer to this distribution of wetting phase as "clusters" as the wetting phase is likely still continuous through wetting films and pendular liquid. Evidently, the rate of displacement has an effect on the final distribution of wetting phase even for nominally stable displacements.

For displacements with M above 10, significant wetting phase remains at the microscopic scale even after significant volumes of displacement phase have swept the pore space. Note the relatively high frequency of white shading, representing wetting phase, in the microscopic images. There again appears to be a Ca dependence on the distribution of the wetting phase. Examine the summary in Fig. 27 at M of 31 and 54. At low Ca, the wetting phase is distributed uniformly and in small pockets. At the largest Ca of about 7×10^{-6}, the wetting phase saturation pockets are larger in size although still rather uniformly distributed. The uniform distribution is likely a result of the micromodel structure that is itself quite regular.

Figure 28 presents the trend of irreducible wetting liquid saturation in the entire micromodel versus Ca. Evidently, $1 - S_w$ is the nonwetting phase that has been embedded in the pore space. The trend in the microscopic images of decreasing wetting phase saturation as Ca increases is clear here.
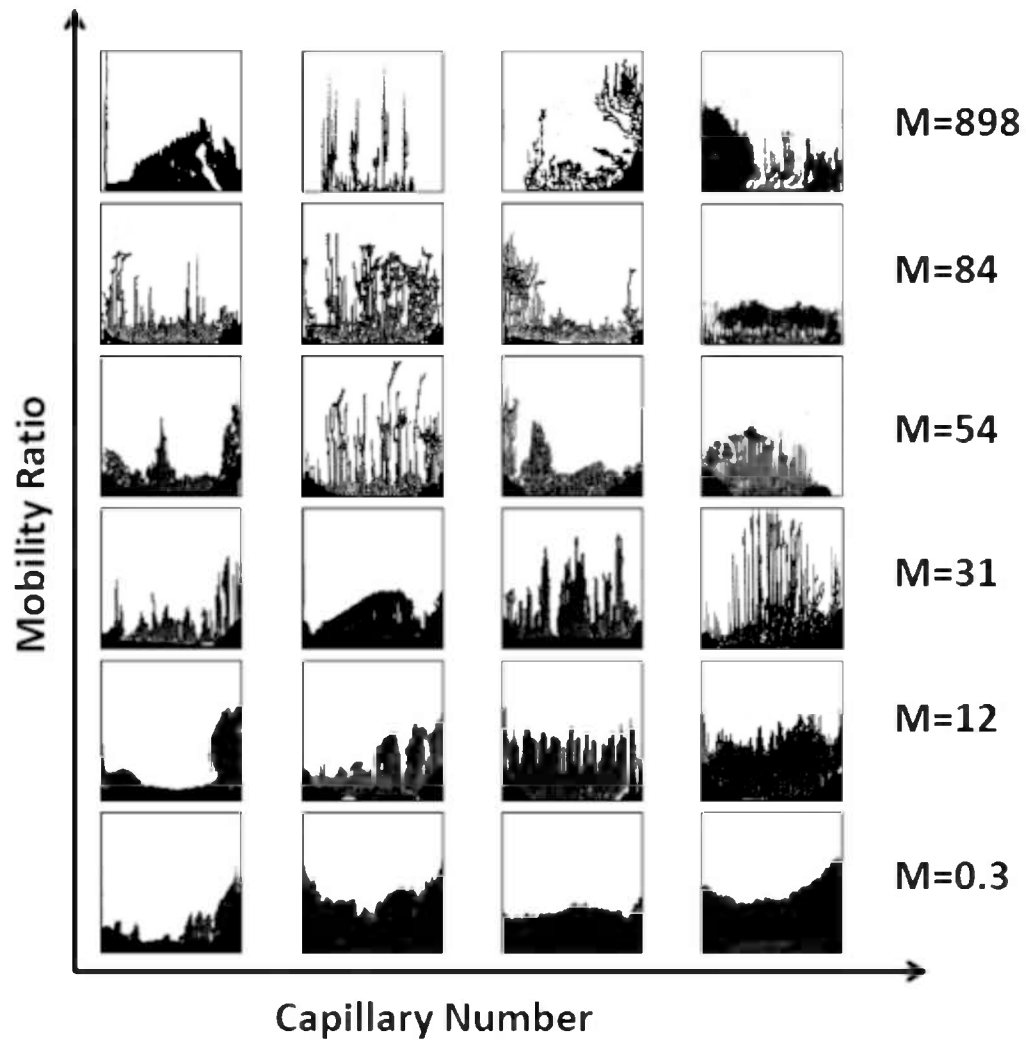
Figure 26: Characteristic displacement patterns during drainage. The view is of the saturation distribution in the whole micromodel. The nonwetting phase is black and pores and wetting phase are white.
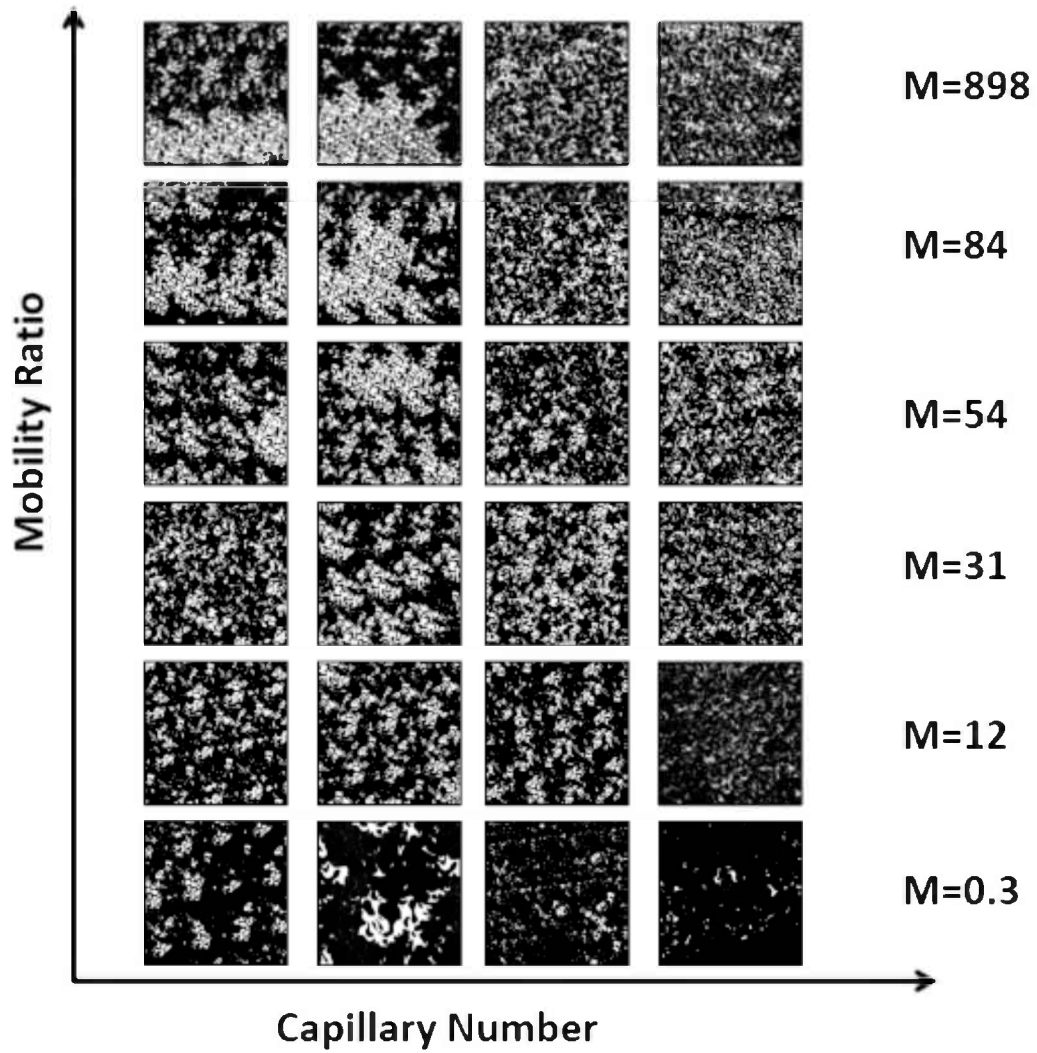
Figure 27: Characteristic distribution of fluids at the pore level at steady state. The view is of an ensemble of pores in the micromodel. The magnification is roughly 40X. Wetting phase is shaded white and the invading nonwetting phase is darkly shaded.
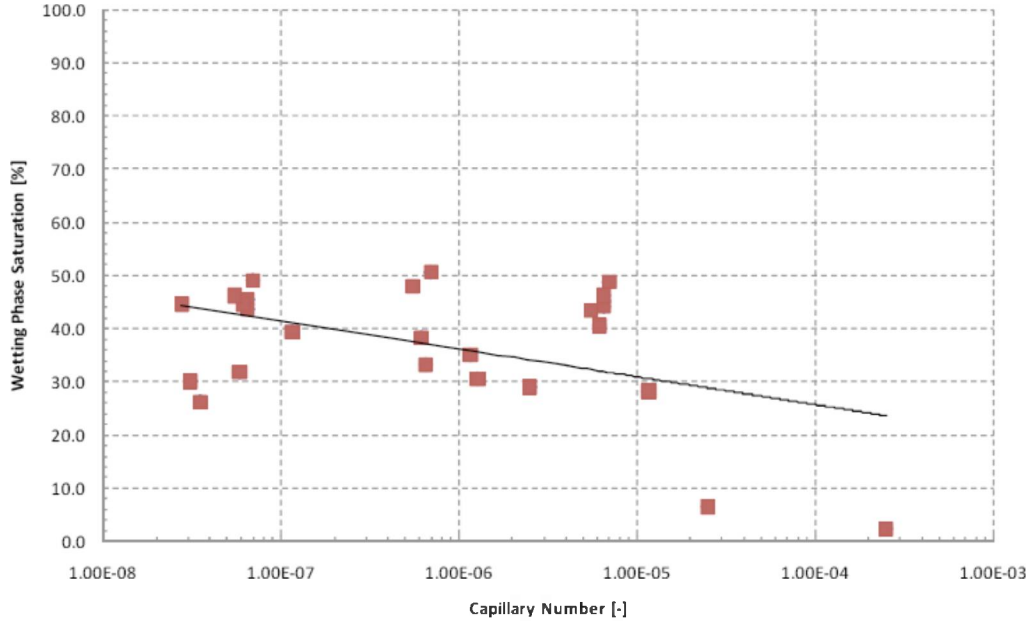
Figure 28: Trend of irreducible wetting phase saturation versus capillary number for all experiments.

Drainage results – CO_2 and water

Given the superior images obtained while using the UV dye in the wetting phase, we extended the experimental technique to consider its applicability when CO_2 was the nonwetting phase. These are low pressure experiments and CO_2 is in the gas phase. The M for these displacement is equal to 62.5. The procedures followed are similar to those above using the matched viscosity ratio fluids except that rather than injecting CO_2 at constant rate, we inject at a constant pressure drop across the micromodel. By increasing the pressure drop, the flow rate is increased. Pressure drops of 6895 Pa (1 psi), 13789 Pa (2 psi), and 20684 Pa (3 psi) were examined. These pressure drops result in Ca of $3.14 \times 10^{-8}, 8.47 \times 10^{-8}$, and 1.59×10^{-7}, respectively, as determined by the steady state flow of CO_2 through the micromodel.

Results are presented in Figs. 29 to 30. The injected CO_2 is black in these images similar to all of the drainage displacements reported above. Figure 31 at the greatest Ca presents saturation profiles that are qualitatively similar to the results with matched viscosity ratio fluids. That is, multiple finger-like features that are relatively narrow and span about one third to two thirds of the length of the micromodel. The displacements in Figs. 29 and 30, however, are somewhat different in comparison to the previous results. Few fingers emerge and those that do, Fig. 29 (B) to (D), are substantially wider. Additionally, all tests in these series display preferential flow along the edges of the domain.

At this stage, we are uncertain as to the reasons for the differences among CO_2/brine and oil/water drainage displacements. The likely explanation is that the injection conditions are different, constant pressure versus constant rate, resulting in somewhat

38

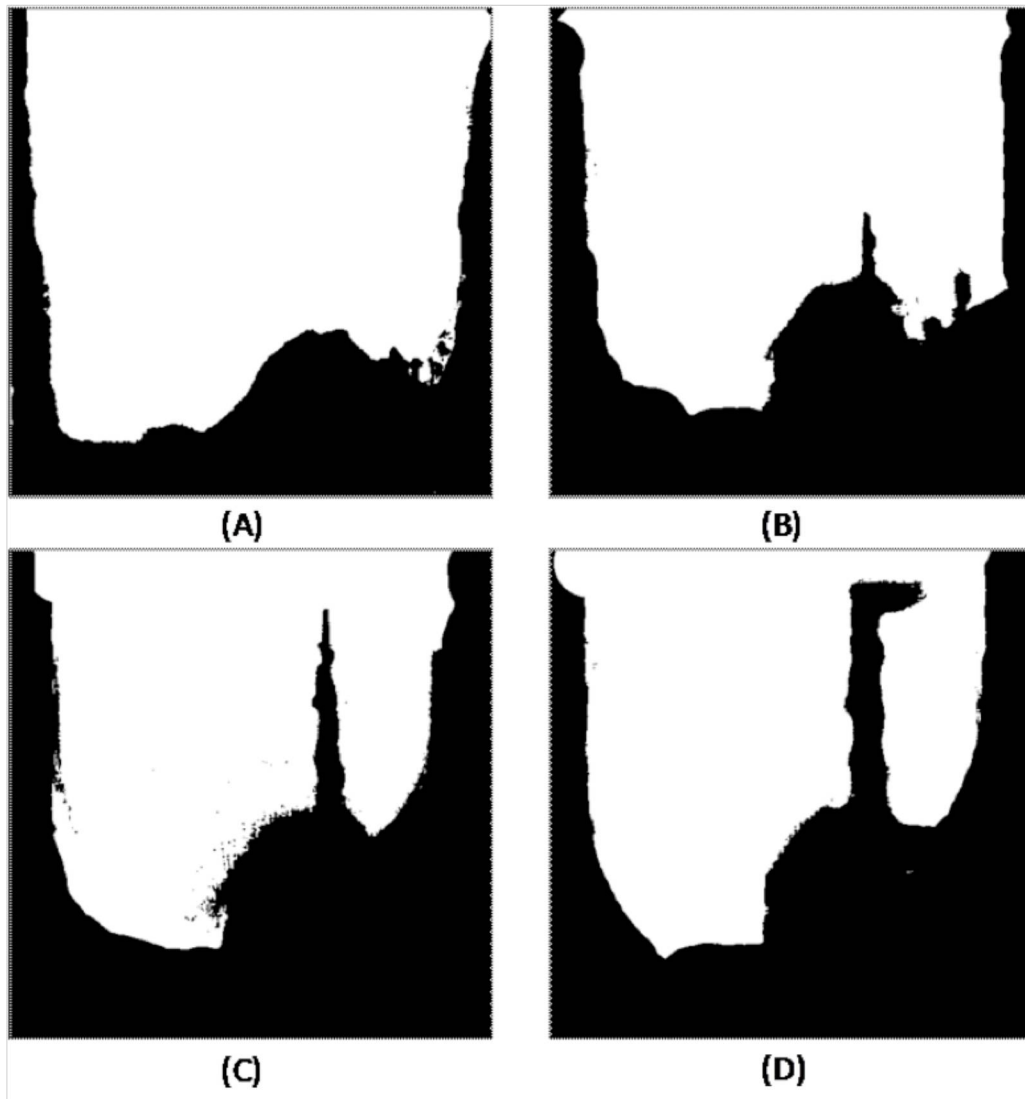different pore-level displacements that cascade to the larger scale.

Figure 29: Drainage displacement results at $M = 62.5$ and $Ca = 3.14 \times 10^{-8}$. The nonwetting phase is CO_2. (A) 30:00 (min:sec) , (B) 108:00, (C) 127:00, (D) 156:00.
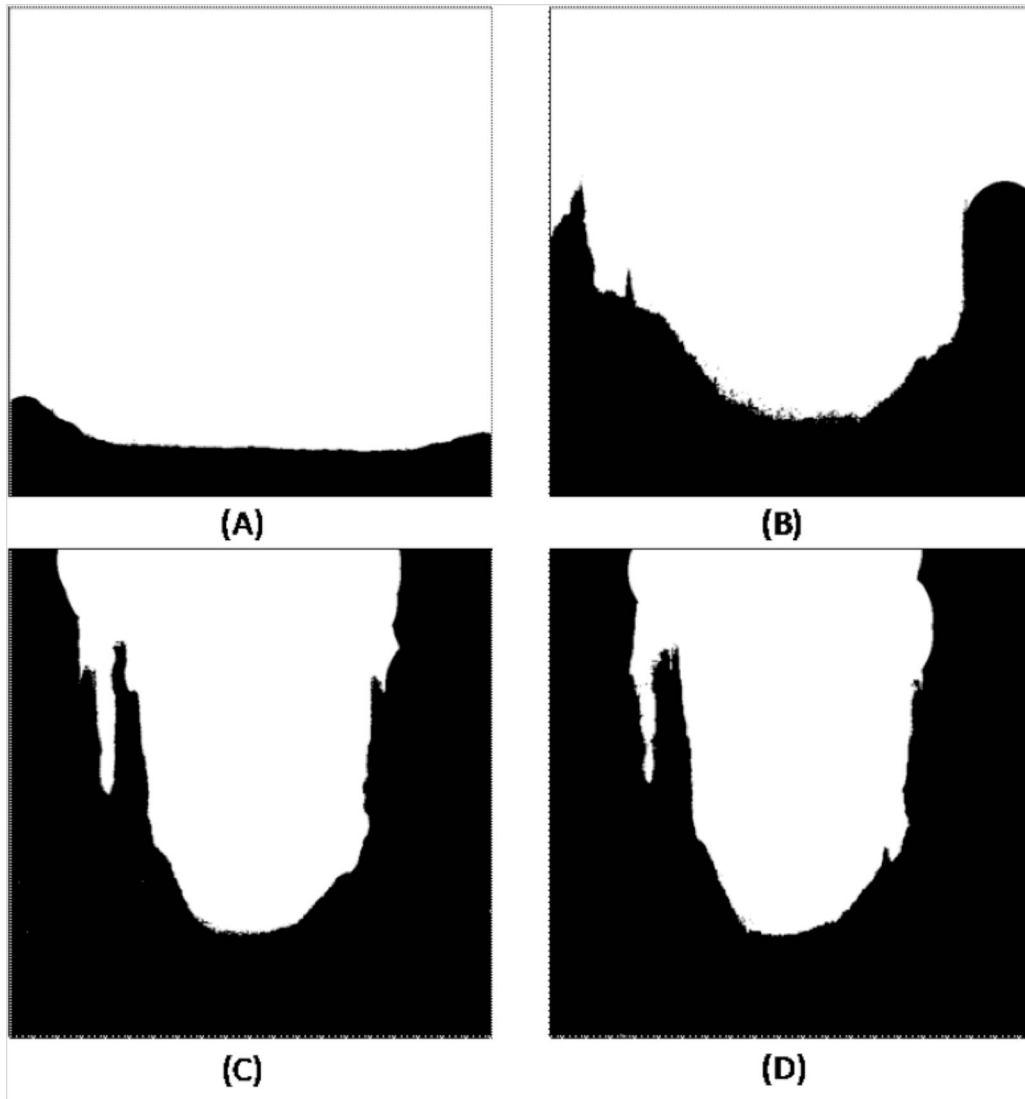
Figure 30: Drainage displacement results at $M = 62.5$ and $Ca = 8.47 \times 10^{-8}$. The nonwetting phase is CO_2 (A) 25:00 (min:sec), (B) 46:00, (C) 74:00, (D) 101:00.
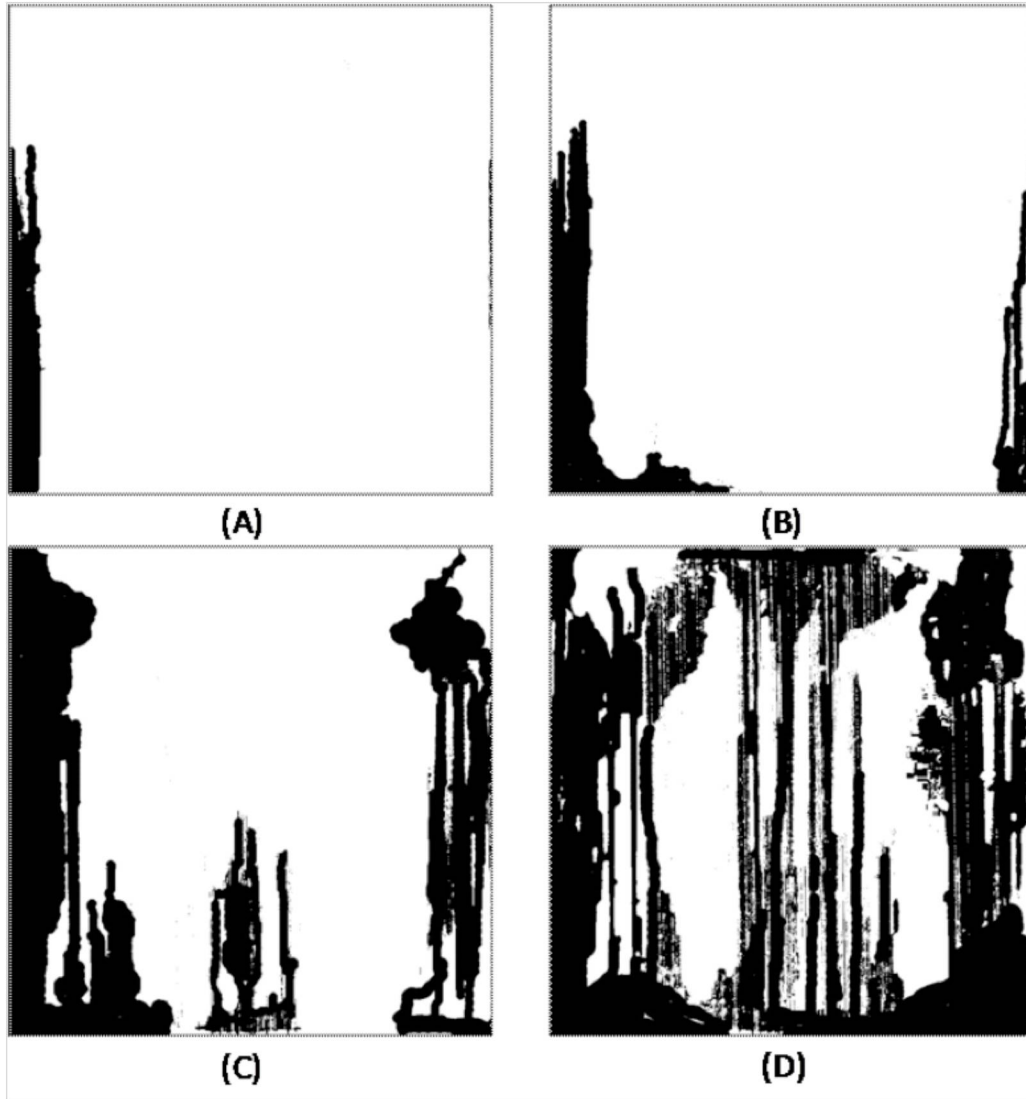
Figure 31: Drainage displacement results at $M = 62.5$ and $Ca = 1.59 \times 10^{-7}$. The nonwetting phase is CO_2 (A) 00:40 (min:sec), (B) 1:00, (C) 1:22, (D) 1:43.

Computational Level-Set Method for Two-Phase Flow in Porous Media

Introduction

The computational investigation also focused on the pore scale. Our computational objectives were to:

1. develop a computational method for simulating two-phase flows in arbitrary rock geometry and

2. investigate the physical mechanisms occurring at the pore-scale, specifically the influence of the geometry of the rock structure as well as the viscous, capillary, and gravitational forces and their effect on the flow regimes.

Multiphase flows in arbitrary geometries present a real challenge from the point of view of computation. One of the main challenge is the multiscale nature of the phenomena and the limitation of computer resources. To address this challenge we have developed a computational method capable of capturing small length scales while minimizing the computational footprint. In particular, we have further developed the Octree adaptive mesh refinement framework for solving the two-phase flow problem. In addition to the multiscale nature of multiphase flows in porous media, the complex geometry of the porous medium as well as the complex interface between fluids significantly complicate the design of accurate and efficient computational strategies. We have used a level-set approach to keep track of the interface between fluids and an implicit representation of the rock's geometry. We have then focused on applying boundary conditions in a physically accurate 'sharp' fashion, i.e. we do not arbitrarily smear the physical quantities across the interface between fluids or at the rock's boundary. Using this general framework and its variants, we have studied the effects of capillary, viscosity and gravitational forces as well as the effect of the rocks geometry. We are in the process of validating our approach on complex geometries. Several techniques have been developed to provide an efficient solver.
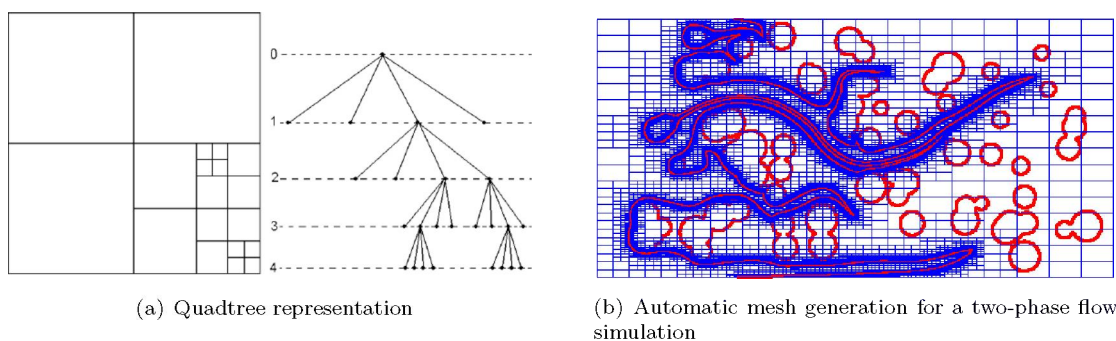
(a) Quadtree representation

(b) Automatic mesh generation for a two-phase flow simulation

Figure 32: Adaptive mesh refinement framework of (21).

Adaptive Mesh Refinement on Octree-Based grids for Two-Phase Flows

One of the difficulties in developing a two-phase flow method on pores structures is that the grids do not necessarily align with the geometry of the pores. One approach is to devise complex meshing procedures, such as those used in finite element methods. However, a drawback is that the quality of the mesh directly influences the accuracy of the solver and, while progress have been made on mesh generator, it is still an open research topic. Another approach is to use smeared out interface methods such as the immersed boundary or so-called delta-formulations. A appealing feature is its simplicity, but those methods have limitations of their own, mainly the lack of accuracy near interfaces or rock's geometry where the accuracy most matters. We have thus design an approach that allows the discretization of arbitrary geometrical shape pores in a sharp boundary framework. Cartesian grids are thus considered and the multiscale nature of two-phase flows in porous media is addressed using adaptive mesh refinement techniques.

The basic idea behind adaptive mesh refinement (AMR) is to refine regions of the computational domain in which high resolution is needed to resolve developing features, while leaving less interesting parts of the domain at lower resolutions (see figure 32). PI Gibou has introduced a novel paradigm for solving partial differential equations on highly versatile Octree grids. In fact, this approach does not limit the ratio between adjacent cells so that mesh refinement is versatile, straightforward, efficient and robust for a wide range of applications (21; 20; 22; 6; 5). We have also developed numerical methods to consider arbitrary geometries, the effect of surface tension, viscosity difference between fluids, viscosities and different fluid' densities. This framework has been applied to the simulation of two-phase flows in porous media, as illustrated in figure 33.

Computational Level-Set Framework

Contact-Line Dynamics

In the context of level set methods, several investigators have recently reported on computational analysis of two-phase flows with moving contact lines (18; 32; 35). Liu
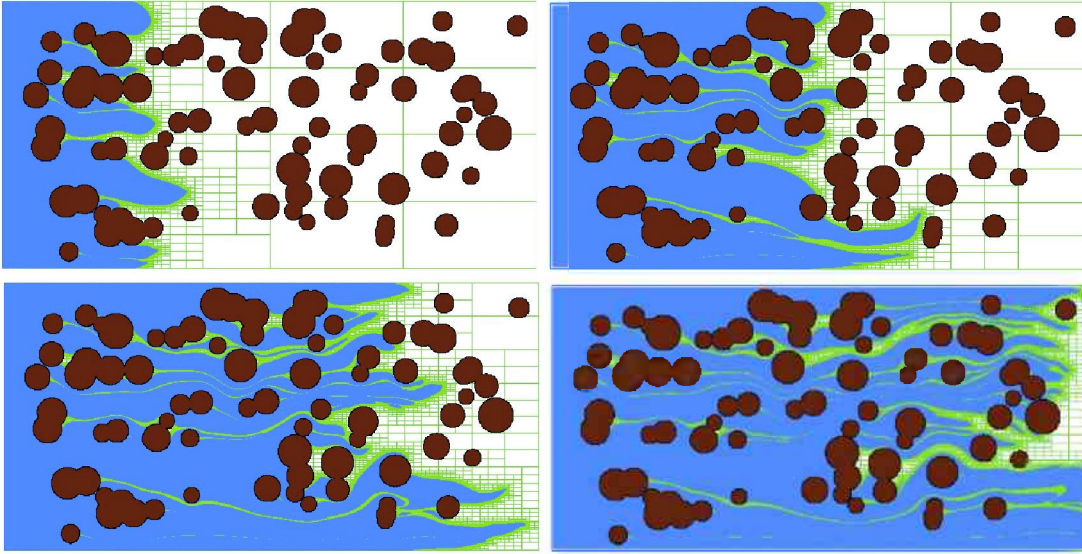
Figure 33: Simulation of two-phase flows in porous media at different time (from left to right and top to bottom). The blue fluid is less viscous than the white fluid triggering viscous fingering effects. The adaptive mesh is represented in green. The arbitrary rock structure is represented in brown.

et al. (18) studied droplet impact and spreading on surfaces of arbitrary shape. They applied the Navier slip boundary condition at the vicinity of the contact line but not along the rest of the wall. As noted by Miksis (19), this would still lead to a singular stress at the contact line, yet their results appear to be in reasonable agreement with experiments. To enforce the contact angle boundary condition, Liu et al. also had to use an explicit interface reconstruction procedure independent of the physical flow field. A more thorough study was presented by Spelt (32), in which he imposed the Navier slip boundary condition along the entire wall together with a relation between the dynamic contact angle and the contact line velocity, to simulate the deformation of a droplet in a creeping shear flow. The author also investigated in details the convergence properties of the method and the regularization of the stress singularity. He showed that the use of discretization errors to introduce numerical slip would result in a maximum shear rate that increases rapidly under mesh refinement.

In a recent systematic study by Ren and E (28), reconciling molecular dynamics and continuum theory, the authors proposed a new effective boundary condition for moving contact lines. They suggested that the Navier slip boundary condition should be imposed away from the contact line, while at the contact line they derived a modified boundary condition by balancing the friction force inside the contact line region with the uncompensated Youngs stress, which results from deviation of the contact angle from its static value. Their effective boundary condition can be expressed as:

1. at the wall, away from the contact line: $\beta \mathbf{u} = \mu \frac{\partial \mathbf{u}}{\partial z}$,

2. at the contact line: $\beta_{CL} \mathbf{u}_{CL} = \sigma \left(\cos(\theta_s) - \cos(\theta) \right)$,

where, β and β_{CL} represent friction coefficients at the surface and contact line, re-

(a) $Ca = \infty$

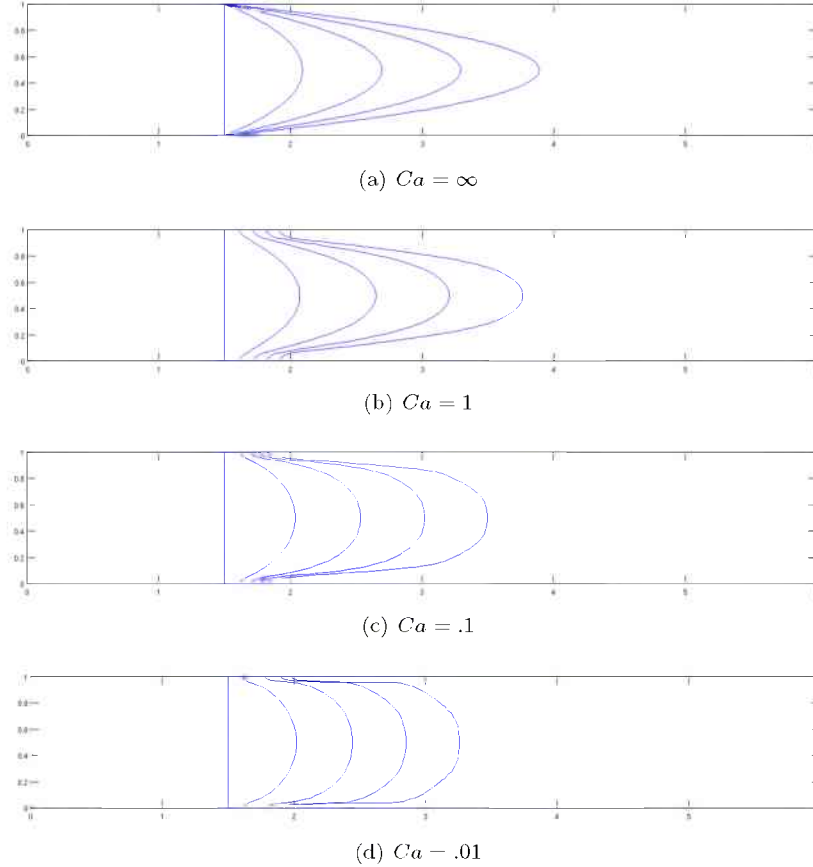(b) $Ca = 1$

(c) $Ca = .1$

(d) $Ca = .01$

Figure 34: Evolution of the interface between two fluids at $t = 0, 0.5, 1, 1.5$, and 2 for different Ca numbers. The static contact angle $\theta_s = \pi/8$.

spectively, z is the vertical coordinate normal to the wall, σ is surface tension, μ is viscosity, and θ and θ_s are the instantaneous and static contact angles, respectively.

An example of the simulation of a two-phase flows with imposed contact angle is depicted in figure 39. We have shown that our framework is capable of imposing the desired contact angle in our simulation.

Results and Discussion

The first part of this study focused on implementation of the level-set method, the CSF, continuum-surface-force, formulation for surface tension and the modified boundary condition at the contact line, in an existing in-house CFD code for single phase flows. We consider the Bretherton problem (3), with an interface separating two fluids of matching densities and viscosities in a Hele-Shaw cell. The apparent contact angle is initially $\pi/2$ and we assume a fully developed Poiseuille velocity profile at the inlet. Preliminary results (see figure 34) show that the Ca number has a major effect on the interface propagation and the dynamics of the moving contact
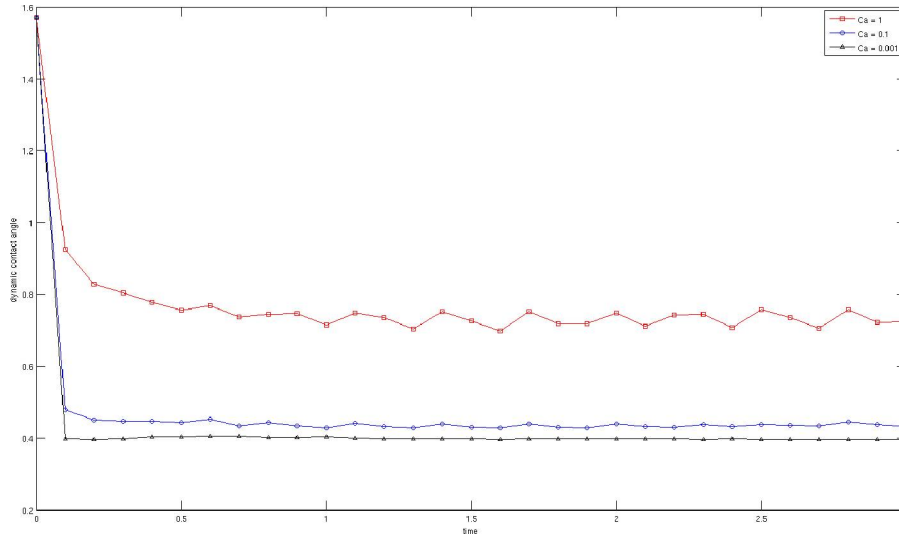
Figure 35: Effect of the Ca number on the dynamic contact angle. The static contact angle is $\theta_s = \pi/8$.
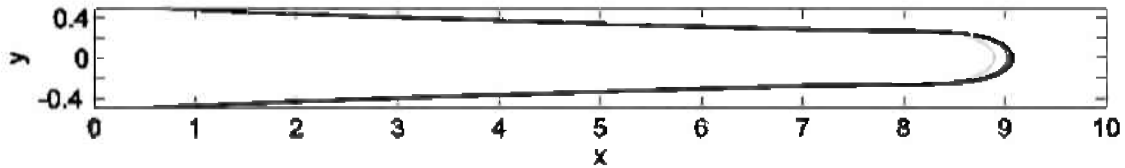

Figure 36: Convergence of the finger shape under grid refinement for a uniform grid of size $400 \times 40, 800 \times 80, 1000 \times 100$ and 1200×120 (light gray to black). ($Re = 1, Ca = 1, \mu_2/\mu_1 = 2$).

line. In figure 35 we see that the difference between the dynamic and static contact angle decreases for smaller Ca numbers.

In the second part of this project, we adopted a different CFD code, originally developed in our lab for miscible two-phase flows, because it has the capability of handling fluids with different viscosities and thus it allows us to investigate the effect of finite viscosity ratios on viscous fingering. The code was modified for immiscible two-phase problems, and the level set method and surface tension formulation were implemented. Although some results are shown here, extensive work on the validation of the code is still being performed. To confirm the grid convergence of the finger shape, we compared the evolution of the finger for different grid sizes as illustrated in figure 36. There is very little difference between the results of the two finest grids, so we used a grid of 1000×100 for all the cases presented next. A parametric study was carried out to determine the effects of the Capillary number, $Ca = U\mu_1/\sigma$, and the viscosity ratio μ_2/μ_1. For all the results presented here Reynolds number, $Re = \rho U b/\mu_1$, was kept at $Re = 1$. In figure 37 the evolution of fingers every 0.5
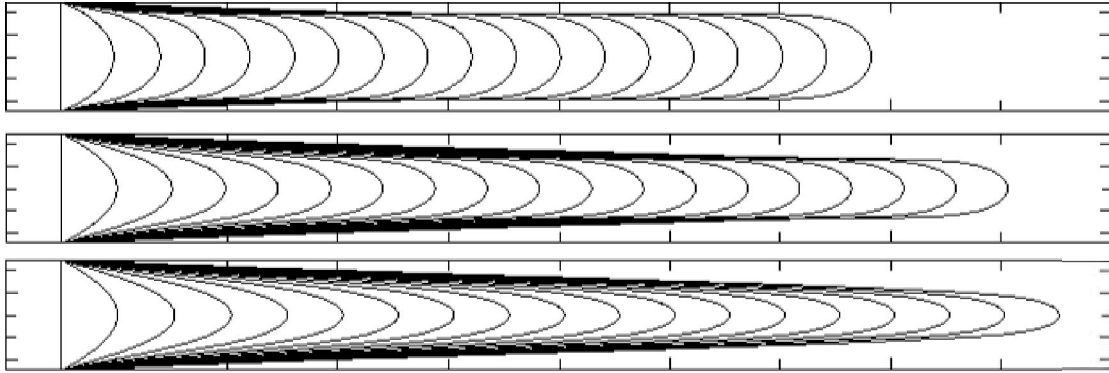
46

Figure 37: Finger evolution for different Ca numbers. From top to bottom $Ca = 0.1, 1, 10$. ($\Delta t = 0.5$, $\mu_2/\mu_1 = 2$).

dimensionless time with $Ca = 0.1, 1, 10$ is depicted. Here the Re number and viscosity ratio were kept constant ($Re = 1$ and $\mu_2/\mu_1 = 2$). For small Ca numbers, surface tension force is dominating and the finger is wider, but its tip velocity is smaller. Its difficult to get accurate quantitative estimates of the steady state film thickness from current results, and a longer domain is needed especially for large Ca numbers. Figure 48 shows the effect of the viscosity ratio on finger evolution with $\mu_2/\mu_1 = 1, 2, 10$ and 20.

We have also starting the investigation of the effect of the Ca number, the contact angle and the viscosity ratio between fluids in the case where the computational domain is not a straight channel. Preliminary results are given in figures 41 and 40. For future work, we plan to extend our investigation to a wider range of parameter space and in particular to the case of arbitrary geometries such as that depicted in figure 33. In particular, we are planning to investigate the effect of the Ca number, the viscosity ratio μ_2/μ_1 (for moderate and large ratios), the Bo number and the effect of the contact angle. Future investigations will focus on regularly and irregularly spaced pore structures such as that depicted in figure 33.
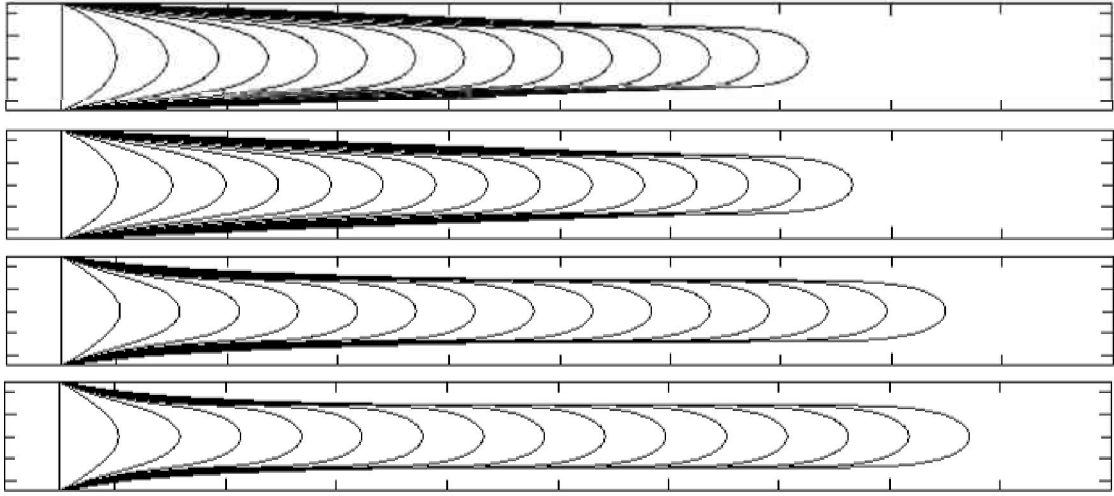
47

Figure 38: Finger evolution for different viscosity ratios. From top to bottom $\mu_2/\mu_1 = 1, 2, 10, 20$. ($\Delta t = 0.5$, $Ca = 1$).
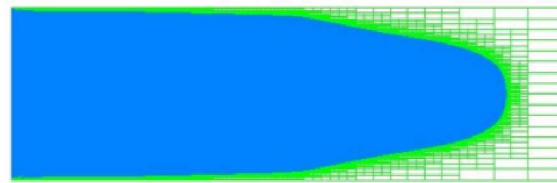
(a) $\theta_s = 0$
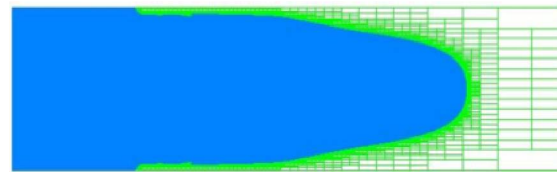
(b) $\theta_s = 90$
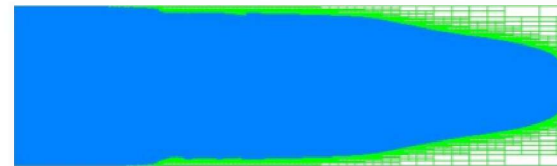
(c) $\theta_s = 120$

Figure 39: Influence of the contact angle θ_s in the simulation of two-phase flows in a channel.
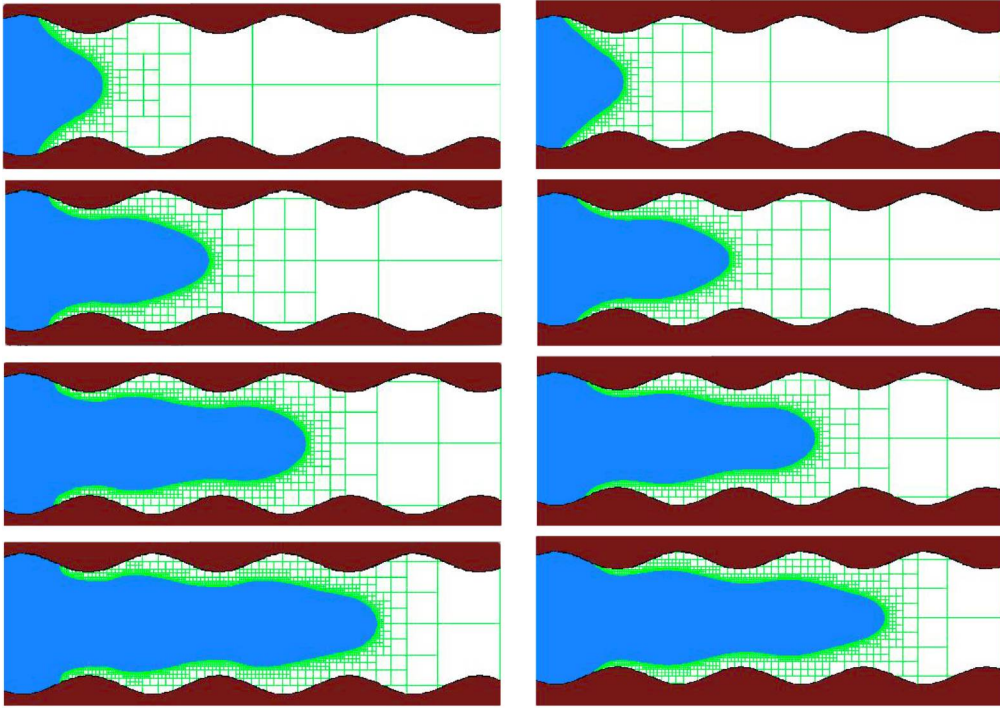
Figure 40: Finger evolution for different viscosity ratios. Each column corresponds to the time evolution. The left column corresponds to $\mu_1/\mu_2 = 100$ and the right column corresponds to $\mu_1/\mu_2 = 1$. In all cases we set $\theta_s = \pi/8$ and $Ca = 1$.
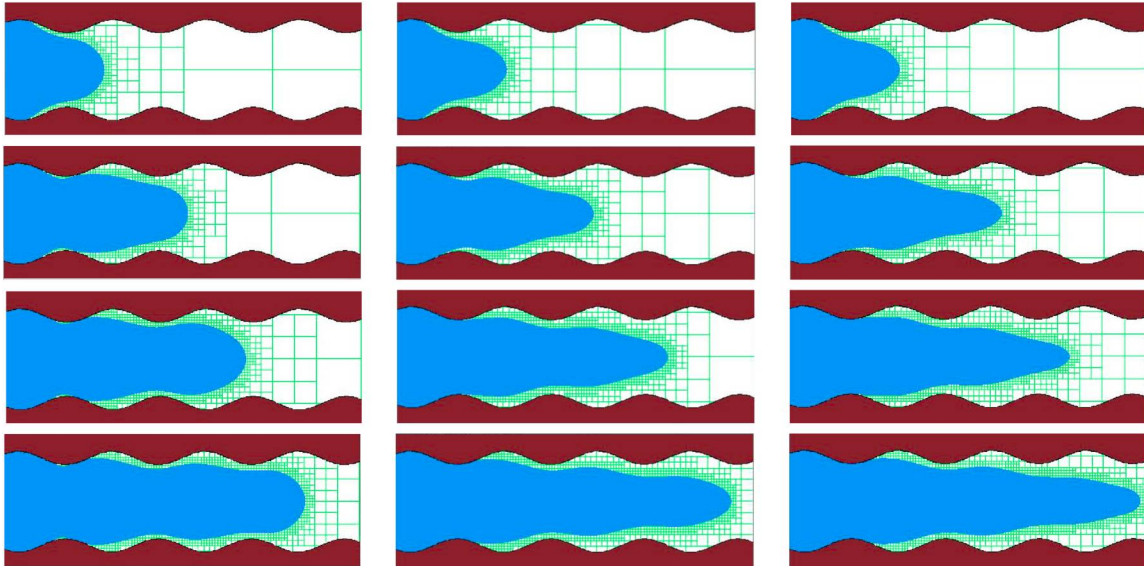
Figure 41: Finger evolution for different Ca. Each column corresponds to the time evolution. The left column corresponds to $Ca = .01$, the middle column corresponds to $Ca = .1$ and the right column corresponds to $Ca = 10$. In all cases we set $\theta_s = \pi/8$ and $\mu_1/\mu_2 = 2$.

Upscaling pore-scale physics to the Darcy scale

The standard Darcy model for single and two phase flow in porous media can be obtained primarily on the basis of either volume averaging with a two-scale expansion (33; 10) or homogenization via multiple scale expansion (2; 23). Several simplifying assumptions are required in both approaches to produce the widely used standard model such as the periodicity of the pore structure, separation of the scales, hydrodynamic stability and pore scale equilibrium. Furthermore, upscaling interfacial dynamics arising from surface tension, jumps in the normal and tangential viscous stresses and the presence of surface viscosity and elasticity may require a fundamental shift away from the typical Darcy model (30; 11; 9).

Our effort for the scale-up of pore scale physics to the Darcy scale is focused on the development of an upscaling framework that attempts to construct Darcy scale conservation laws for momentum transport on the basis of the volume averaging of Navier-Stokes equation. We require that the resulting constitutive relations are general which can be quantified with available experimental and numerical techniques. In order to illustrate this approach in a clear manner we will focus the discussion on incompressible fluids that do not undergo phase change through either thermodynamic or geochemical effects. These can be easily incorporated once the basic framework is available.

We find that the classical approach based on the volume averaging theorem is deficient even for the single phase Darcy model which is improved with the addition of measurable pressure and velocity gradient terms on the surface of the control volume. Based on this model, dependence of the components of the permeability tensor on the governing parameters of capillary number, viscosity ratio and Bond number can be linked rigorously to phase saturation. The traditional form of the Darcy's model with tensorial permeability is hence placed on a solid foundation. The model is exact with respect to the averaged form of the Navier-Stokes equation in so far as all the appropriate terms are measured at the surface of the control volume, which could be a laboratory core.

Volume averaging

Our averaging approach is as follows, we consider the volume average of the Navier-Stokes equation over a region, Ω, first for a single incompressible fluid of constant

density and viscosity,

$$\int_{\Omega} (\rho \mathbf{u}_t - \nabla \cdot \tau) \, \mathrm{d}V = 0 \quad , \quad \tau = -P\mathbf{I} + \mu \left(\nabla \mathbf{u} + \nabla \mathbf{u}^T \right) - \rho \mathbf{u}\mathbf{u} \, , \tag{5}$$

where $\mathbf{I}$ is the unit tensor, V is the volume of region enclosed by Ω and ρ, μ and $\mathbf{u}$ are, respectively, the fluid density, viscosity and velocity. Subscript t indicates the time derivative. By defining volume average quantities,

$$\bar{\mathbf{u}} = \frac{1}{V} \int_{\Omega} \mathbf{u} \, \mathrm{d}V \quad \text{and} \quad \bar{\tau} = \frac{1}{V} \int_{\Omega} \tau \, \mathrm{d}V \quad , \tag{6}$$

Eq. (5) can be expressed as

$$\rho \bar{\mathbf{u}}_t = \frac{1}{V} \int_{\Omega} \nabla \cdot \tau \, \mathrm{d}V = \frac{1}{V} \int_{\Gamma_s} \mathbf{n}_s \cdot \tau \, \mathrm{d}S + \frac{1}{V} \int_{\Gamma_e} \mathbf{n}_e \cdot \tau \, \mathrm{d}S \tag{7}$$

where Γ_e and Γ_s are the surfaces of the control volume and the solids within the control volume, respectively. $\mathbf{n}_e$ and $\mathbf{n}_s$ are the corresponding unit vectors directed outwards from the control volume surface and towards the solid surface. S is the surface area. Terms on the right hand side of (7), integrals of τ normal to the surfaces, is obtained by the application of the divergence theorem to the term in the center, integral of the divergence of τ over the volume.

Application of the spatial averaging theorem of Slattery (33; 31; 12), based on an approximation derived from the Leibniz theorem, can be used to convert the first term on the right hand side of (7) yields, $\int_{\Gamma_e} \mathbf{n}_e \cdot \tau \, \mathrm{d}S = V \nabla \cdot \bar{\tau}$. Equation (7) can then be expressed as

$$\rho \bar{\mathbf{u}}_t = \nabla \cdot \bar{\tau} + \frac{1}{V} \int_{\Gamma_e} \mathbf{n}_e \cdot \tau \, \mathrm{d}S \tag{8}$$

The classical approach to derive Darcy's equation for single phase flow postulates, $\nabla \cdot \bar{\tau} \approx -\nabla \bar{P} \gg \bar{\mathbf{u}}_t$, to arrive at,

$$-\nabla \bar{P} = -\frac{1}{V} \int_{\Gamma_e} \mathbf{n}_e \cdot \tau \, \mathrm{d}S \tag{9}$$

The right hand side is then related to $\mu \mathbf{K} \cdot \bar{\mathbf{u}}$ to produce the standard form of the Darcy's equation for single phase flow,

$$-\nabla \bar{P} = \mu \mathbf{K} \cdot \bar{\mathbf{u}} \, , \tag{10}$$

where $\mathbf{K}$ is the permeability tensor.

The spatial averaging theorem is not general and its validity remains inconclusive. The second difficulty is the neglect of time dependence of velocity in Eq. (5), which is justified strictly only for passive tracer flows but is invalid for a moving front separating miscible fluids with unfavorable viscosity and density contrasts, where the local flow field is unsteady.

As a general approach we propose

$$\int_{\Gamma_{\alpha e}} \tau_\alpha \cdot \hat{\mathbf{n}}_{\alpha e} \mathrm{d}S = \nabla \cdot \int_{\Omega_\alpha} \tau_\alpha \mathrm{d}V + \int_{\Gamma_{\alpha e}} \mathbf{D}(\mathbf{u}) \cdot \hat{\mathbf{n}}_{\alpha e} \mathrm{d}S, \tag{11}$$

where $\mathbf{D}$ is a tensor associated with the $\Gamma_{\alpha e}$ surface which can be measured precisely with direct numerical simulations. The spatial averaging theorem with this generalization is applied to Eq. (5) to obtain Darcy's law, $\nabla \cdot \bar{\tau}_\alpha = -\mu_\alpha \mathbf{K}^{-1} \cdot \bar{\mathbf{u}}$, where $\mathbf{K}$ is the permeability tensor given by

$$\int_{\Gamma_{\alpha s}} \tau \cdot \hat{\mathbf{n}}_{\alpha s} \mathrm{d}S + \int_{\Gamma_{\alpha e}} \mathbf{D} \cdot \hat{\mathbf{n}}_{\alpha e} \mathrm{d}S + \int_{\Omega_\alpha} \rho_\alpha \mathbf{u}_t \mathrm{d}V = \mu_\alpha \mathbf{K}^{-1} \cdot \bar{\mathbf{u}} . \tag{12}$$

This is the most general form of Darcy's' law for single fluid system which requires knowledge regarding the rate of strain tensor on pore surfaces which may not always be readily available. However, progress can be made by simplifying the left hand side of Eq. (12) by applying the divergence theorem to Eq. (5) to obtain

$$\mu_\alpha \mathbf{K}^{-1} \cdot \bar{\mathbf{u}} = -\int_{\Gamma_{\alpha e}} (\tau - \mathbf{D}) \cdot \hat{\mathbf{n}}_{\alpha s} \mathrm{d}S \tag{13}$$

providing a clear relationship between permeability and measurable flow quantities at the entrance and exit surfaces of the averaging volume. Thus the traditional form of the single fluid phase Darcy's law with tensorial permeability is placed on a solid foundation. The model described by Eq. (13) is exact and does not contain any approximations in so far as all the appropriate terms are measured at the surface of the control volume, which could be a laboratory core.

In order to demonstrate the behavior of velocity and pressure averaged over an arbitrary control volume, Fig. 42(a) plots the streamwise steady-state velocity (normalized by the maximum value) resulting from the uniform flow imposed at $x = 0$ through solid, circular obstacles of diameter, $d_s = 1/40$, in two circular averaging volumes of diameter, $d_V = 0.4$. The centers of the averaging region, Ω, are located at two different positions at the same instant in time. Velocity outside the averaging region is set to zero to emphasize the flow field inside the averaging volume. In order to determine whether the averaged quantities are differentiable, averages of velocity, $\bar{u}$ and pressure, $\bar{p}$, are obtained in an averaging volume that translates along the path indicated by the dashed line in Fig. 42(a) and are plotted in Fig. 42(b). The averages are normalized appropriately to facilitate comparison. While the pressure average is relatively smooth as compared to the velocity average, differentiability appears to exist for both, at least in the case of single fluid phase flow through homogeneous random porosity.

Multiphase flow upscaling

We can obtain Darcy's law for multiphase flow for the case of two fluid phases from the Stokes equation in a manner similar to that for the single fluid phase case. Averaging
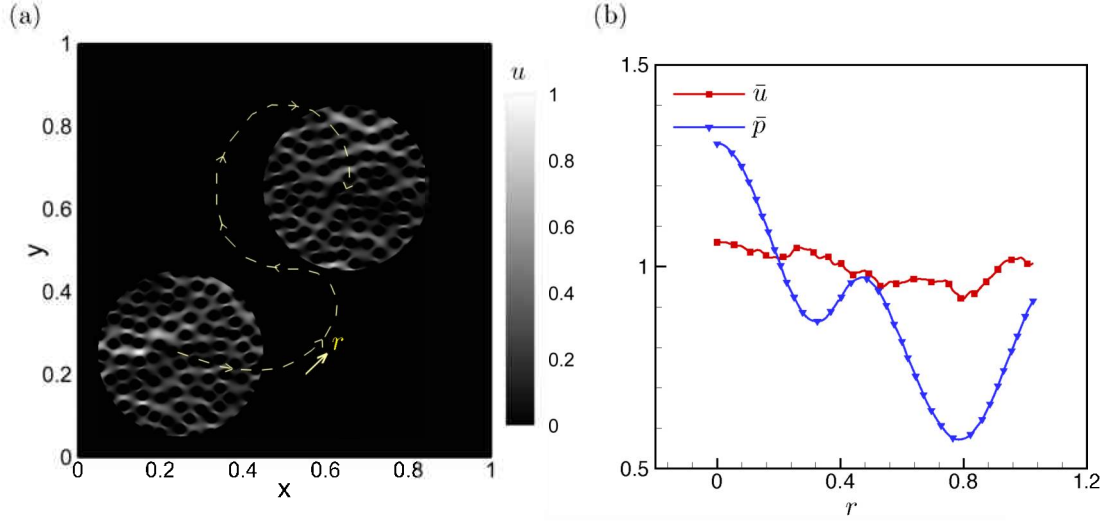
Figure 42: (a) Streamwise, steady-state velocity field, u, (normalized by maximum value) in a random array of circular obstacles (diameter $d_s = 1/40$), plotted within two averaging volumes (diameter $d_V = 0.4$) with centers at different positions at the same instant in time. The dashed line shows the path along which the averaging volume is translated. (b) Average values (normalized to facilitate comparison) of velocity, $\bar{u}$ and pressure, $\bar{p}$, as functions of arc length, r, along the path indicated in (a).

both phases over the region, Ω,

$$\nabla \cdot \bar{\tau}_i = \int_{\Omega_i} \rho_i \mathbf{u}_{i,t} \mathrm{d}V - \int_{\Gamma_{is}} \tau_i \cdot \hat{\mathbf{n}}_{is} \mathrm{d}A - \int_{\Gamma_{ij}} \tau_i \cdot \hat{\mathbf{n}}_{ij} \mathrm{d}A , \quad i,j = \alpha, \beta, \cdots , \quad i \neq j , \quad (14)$$

where $\tau_i = -P_i + \mu_i \nabla \mathbf{u}_i - \rho_i \mathbf{u}_i \mathbf{u}_i$ is the viscous and inertial stress tensor, Γ_{ij} is the fluid-fluid interface, $\mathbf{u}_{i,t}$ indicates the time derivative of the ith phase and subscripts ii do not indicate summation. Making use of divergence and Leibniz theorems the integrals over fluid-fluid and fluid-solid interfaces to be expressed as integrals over the open surfaces, Γ_{ie}, which enables us to postulate

$$- \int_{\Gamma_{\alpha e}} (\tau_\alpha - \mathbf{D}_\alpha) \cdot \hat{\mathbf{n}}_{\alpha e} \mathrm{d}A = \mu_\alpha \tilde{\mathbf{K}}_{\alpha\alpha}^{-1} \cdot \bar{\mathbf{u}}_\alpha + \mu_\beta \tilde{\mathbf{K}}_{\alpha\beta}^{-1} \cdot \bar{\mathbf{u}}_\beta , \qquad (15)$$

$$- \int_{\Gamma_{\beta e}} (\tau_\beta - \mathbf{D}_\beta) \cdot \hat{\mathbf{n}}_{\beta e} \mathrm{d}A = \mu_\beta \tilde{\mathbf{K}}_{\beta\beta}^{-1} \cdot \bar{\mathbf{u}}_\beta + \mu_\alpha \tilde{\mathbf{K}}_{\beta\alpha}^{-1} \cdot \bar{\mathbf{u}}_\alpha , \qquad (16)$$

which can be rearranged in a form similar to the standard multiphase Darcy's law, $\bar{\mathbf{u}}_i = -\mathcal{K}^{ij} \cdot \nabla \cdot \bar{\tau}_j$, where i and j indicate fluid phase and $\mathcal{K}$ is the multiphase permeability tensor that relates the divergence of average phase stress, $\bar{\tau}_i$, to the averaged velocities, $\bar{\mathbf{u}}_i$, for each phase. In general, $\mathcal{K}$ is a tensor of order $m \times n$, where m is the number of phases and n is the system dimensionality, while the tensors $\tilde{\mathbf{K}}$ are of order n. Eqs. (15) and 16 reflect the assumption that stress is linearly proportional to velocity while tensors $\tilde{\mathbf{K}}_{\alpha\beta}^{-1}$ and $\tilde{\mathbf{K}}_{\beta\alpha}^{-1}$ are inserted to represent

53

the effect of momentum coupling between the two fluid phases due to flow along fluid-fluid interfaces. This formulation allows the phase permeability tensors, $\tilde{\mathbf{K}}^{ij}$, to be determined at a fundamental level as integrals of fluid dynamic stresses either at the phase interfaces in the interior of the averaging volume or along the open surfaces that enclose the averaging volume. Note that all information related to fluid-fluid interfaces, such as interfacial area, jump conditions, contact line motion and interfacial elasticity and viscosity is represented implicitly by the $m \times n$ components of the m^2 relative permeability tensors. Methods of introducing non-equilibrium and unsteady state effects into the permeability tensors will be investigated on the basis of multidimensional expansions noted in § ??, for saturation as well as velocity and pressure variables.

This model of multiphase flow is the most general expression of the phase interaction in an averaging volume. The classical form of Darcy's law is recovered only for isotropic flow by separating the effects of fluid-fluid and fluid-solid interactions as $\tilde{\mathbf{K}}^{ii} = k_{ii}k\mathbf{I}$, for $k_{\alpha\beta} = 0$ and $k_{\beta\alpha} = 0$, leading to $\bar{\mathbf{u}}_i = -k_{ii}k\nabla \cdot \bar{\tau}_i$, where k_{ij} are the scalar relative permeability functions, k is the scalar absolute permeability and $\mathbf{I}$ is the unit tensor. In case $k_{\alpha\beta} \neq 0$ and $k_{\beta\alpha} \neq 0$, or the absolute permeability has a tensorial form, the contribution to individual components of $\mathcal{K}^{ij}$ cannot be segregated into effects arising from a single phase. In order words, components of $\mathcal{K}$ are complicated functions of k_{ij} and the components of the absolute permeability tensor, $\mathbf{K}$. Therefore, it is not possible to justify the standard form of multiphase Darcy's law, $\bar{\mathbf{u}}_i = -k_{ij}\mathbf{K} \cdot \nabla \cdot \bar{\tau}_j$, rigorously on the basis of the averaged Stokes equations (34; 17). This formulation also clarifies the earlier inconsistency regarding relative permeability values greater than unity, which is due to the artificial segregation of the effects of single and multiple fluid phase permeability, although it is generally true that the lubrication effect lowers the resistance in an annular multiphase flow.

In order to employ the current form of Darcy's law for practical purposes the dependence of the components of the relative permeability tensor on the governing parameters of capillary number, viscosity ratio and Bond number will be determined along with their dependence on the phase saturation and the fluid-fluid and fluid-solid interfacial area. The components $\tilde{\mathbf{K}}^{ij}$ will be determined by a treatment similar to that of the single phase flow, i.e. by subjecting the averaging control volume to $m \times n$ independent flow configurations to determine the $m \times n$ unknowns, based on the data obtained from our numerical simulations and experiments. We would also test whether the decomposition, $\tilde{\mathbf{K}}^{ij} = \mathbf{K}^{ij} \cdot \mathbf{K}$, may be useful, where $\mathbf{K}^{ij}$, can be understood as the true relative permeability tensor which in general is full.

Conclusions

CO_2 sequestration operations involve complex multi-component multiphase interactions that are not fully understood. The super-critical CO_2 is expected to be immiscible with the resident brine with very large density and viscosity contrasts between the two phases. As a result, complex unstable flows have been reported across a wide range of scales starting with the pore level. If this is indeed the case, then the use of standard Darcy-scale models to represent the multiphase dynamics associated with subsurface CO_2 storage is not appropriate. Thus, developing a fundamental understanding of the pore-scale physics of unstable immiscible flow in porous media is needed. This research project was aimed at developing such an understanding. The focus was on the detailed pore-scale physics and the development of a framework to model, and ultimately translate, the pore-scale physics to the Darcy and larger scales. The project had substantial experimental and computational components.

The experiments focused on the use of micromodels. Drainage experiments of immiscible two-phase flow were performed. The viscosity ratio, M, varied from highly favorable ($M = 0.3$) to highly unfavorable ($M = 84$). For each viscosity ratio, the capillary-number, C_a, was varied across a wide range. The experiments show that when M is much larger than unity, the flow patterns are quite complex with a wide range of finger length scales. Overall, for a given $M > 1$, the instabilities associated with these immiscible displacements are more benign than their miscible counterparts. Specifically, unlike the miscible setting, immiscible instabilities are rarely dominated by of a few large fingers that bypass the resident fluid. However, the local wetting phase saturation in the flooded regions can be persistently large indicating significant microscopic bypassing. The standard Darcy model for multiphase flow cannot fully capture these observations.

In addition to the multiscale nature of multiphase flows in porous media, the complex geometry of the porous medium and the complex fluid-fluid and fluid-solid interface pose serious modeling and computational challenges. Existing Lattice-Boltzmann models have not been designed to describe the complex solid-fluid and immiscible fluid-fluid contacts, and we decided to employ alternative strategies. To better understand the fluid-flow physics at the pore scale, we employed a level-set method that keeps track of the interface between the two immiscible fluids along with implicit representation of the pore-scale geometry. 'Sharp' conditions at the contact-lines between fluids and at the solid boundaries were employed. The Octree adaptive mesh refinement framework was extended in order to solve this immiscible two-phase problem with reasonably good resolution. Computational results of the effects of capillary,

viscous, and gravitational forces have been performed. Validation of our level-set approach for complex pore-scale rock geometries is ongoing. We also developed novel numerical methods for the pressure equation associated with the Navier-Stokes momentum balance. The formulation, which is obtained using a mass weighted continuity equation, ensures a locally conservative velocity field. The jump conditions of pressure and the normal viscous stresses and the continuity of the interfacial stresses are enforced at fluid-fluid interfaces. Solid boundaries are treated using an immersed boundary method. We have also been developing mathematical and computational approaches to translate the physics of immiscible two-phase flow in the presence of viscosity and density differences from the pore to the Darcy scale. Since a modeling framework will ultimately be necessary in order to design and manage large-scale sequestration projects, there is an urgent need to develop models and constitutive relations that describe the relevant multiscale physics accurately. The experimental findings and the advanced computational methods developed in this research project provide a strong basis for designing and validating constitute relations and models of multiphase flow at the pore and larger (e.g., Darcy) scales.

Bibliography

[1] Alshehri,A.J., E. Sagatov, and A.R. Kovscek, 2009. Pore-Level Mechanics of Forced and Spontaneous Imbibition of Aqueous Surfactant Solutions in Fractured Porous Media SPE 124946, Proceedings of the 2009 SPE Annual Technical Conference and Exhibition, New Orleans, Louisiana, USA, 47 Oct.

[2] Brenner, H. (1980). Dispersion resulting from flow through spatially periodic porous-media. *Phil. Trans. R. Soc. Lond. A-Math. Phys. and Eng. Sci.*, *297*(1430), 81–133.

[3] F. P. Bretherton. The motion of long bubbles in tubes.

[4] Buchgraber, M., Clemens, T., Castanier, L. M., & Kovscek, A. R., 2009. The Displacement of Viscous Oil by Associative Polymer Solutions *SPE Reservoir Evaluation and Engineering*, 14(3) 269-280.

[5] H. Chen, C. Min, and F. Gibou. A level set approach to the numerical simulation of the Stefan problem on non-graded adaptive Cartesian grids. *J. Comput. Phys. (submitted)*.

[6] H. Chen, C. Min, and F. Gibou. A supra-convergent finite difference scheme for the poisson and heat equations on irregular domains and non-graded adaptive cartesian grids. *J. Sci. Comput.*, 31(1):19–60, 2007.

[7] Clavaud, J. B., Maineult, A., Zamora, M., Rasolofosaon, P., & Schlitter, C. (2008). Permeability anisotropy and its relations with porous medium structure. *Journal of Geophysical Research-Solid Earth*, *113*(B1).

[8] Cinar, Yildiray., Riaz, Amir., and Tchelepi, H.A., 2007. Experimental Study of CO_2 injection into Saline Formations, *Society of Petroleum Engineers Journal*, Dec 588-594.

[9] Gray, W., & Miller, C. (2005). Thermodynamically constrained averaging theory approach for modeling flow and transport phenomena in porous medium systems: 1. Motivation and overview. *Advances in Water Resources*, *28*(2), 161–180.

[10] Gray, W. G. (1975). Derivation of equations for multiphase transport. *Chemical Engineering Science*, *30*(2), 229–233.

[11] Gray, W. G., & Hassanizadeh, S. M. (1989). Averaging theorems and averaged equations for transport of interface properties in multiphase systems. *International Journal of Multiphase Flow*, *15*(1), 81–95.

[12] Gray, W. G., & Lee, P. C. Y. (1977). On the theorems for local volume averaging of multiphase systems. *International Journal of Multiphase Flow*, *3*, 333–340.

[13] Greenkorn, R. A., Johnso, C. R., & Shallenberger, L. K. (1964). Directional permeability of heterogeneous anisotropic porous media. *Society of Petroleum Engineers Journal*, *4*(2), 124–132.

[14] Gu, J., 2010. A Microvisual Investigation of Viscously Unstable Displacement for CO_2 Injection, Energy Resources Engineering Department. Stanford University. M.S. thesis.

[15] Inwood, S., 2008. High-Resolution Microvisual Study of High Mobility Ratio, Immiscible Displacements, Energy Resources Engineering Department. Stanford University. M.S. thesis.

[16] Korteland, S., Bottero, S., Hassanizadeh, S. M., & Berentsen, C. W. J. (2010). What is the Correct Definition of Average Pressure? *Transport in Porous Media*, *84*(1), 153–175.

[17] Lasseux, D., Ahmadi, A., & Arani, A. A. A. (2008). Two-phase inertial flow in homogeneous porous media: a theoretical derivation of a macroscopic model. *Transport in Porous Media*, *75*(3), 371–400.

[18] H. Liu, S. Krishnan, S. Marella, and H. S. Udaykumar. Sharp interface cartesian grid method ii: A technique for simulating droplet interactions with surfaces of arbitrary shape.

[19] M. J. Miksis. *Contact lines.* Kluwer Academic Publishers, 2004.

[20] C. Min and F. Gibou. A second order accurate projection method for the incompressible Navier-Stokes equation on non-graded adaptive grids. *J. Comput. Phys.*, 219:912–929, 2006.

[21] C. Min and F. Gibou. A second order accurate level set method on non-graded adaptive Cartesian grids. *J. Comput. Phys.*, 225:300–321, 2007.

[22] C. Min, F. Gibou, and H. Ceniceros. A supra-convergent finite difference scheme for the variable coefficient Poisson equation on non-graded grids. *J. Comput. Phys.*, 218:123–140, 2006.

[23] Mei, C. C., & Auriault, J. L. (1989). Mechanics of heterogeneous porous-media with several spatial scales. *Proc. R. Soc. Lond. A-Math. Phys. and Eng. Sci.*, *426*(1871), 391–423.

[24] Nordbotten, J. M., Celia, M. A., Dahle, H. K., & Hassanizadeh, S. M. (2007). Interpretation of macroscale variables in Darcy's law. *Water Resources Research*, *43*(8).

[25] Nordbotten, J. M., Celia, M. A., Dahle, H. K., & Hassanizadeh, S. M. (2008). On the definition of macroscale pressure for multiphase flow in porous media. *Water Resources Research*, *44*(6).

[26] Parsons, R. W. (1964). Directional permeability of heterogeneous anisotropic porous media - Discussion. *Society of Petroleum Engineers Journal*, *4*(4), 363–364.

[27] Rangel-German, E. R. and A. R. Kovscek, 2006. A Micromodel Investigation of Two-Phase Matrix-Fracture Transfer Mechanisms, *Water Resources Research*, 42, W03401 (2006). doi:10.1029/2004WR003918.

[28] W. Ren and Weinan E. Boundary conditions for the moving contact line problem.

[29] Renard, P., Genty, A., & Stauffer, F. (2001). Laboratory determination of the full permeability tensor. *Journal of Geophysical Research-Solid Earth*, *106*(B11), 26443–26452.

[30] Scriven, L. E. (1960). Dynamics of a fluid interface - equation of motion for newtonian surface fluids. *Chemical Engineering Science*, *12*(2), 98–108.

[31] Slattery, J. C. (1967). Flow of viscoelastic fluids through porous media. *AIChE Journal*, *13*(6), 1066–&.

[32] P. D. M. Spelt. A level-set approach for simulations of flows with multiple moving contact lines with hysteresis.

[33] Whitaker, S. (1966). Equations of motion in porous media. *Chemical Engineering Science*, *21*(3), 291–&.

[34] Whitaker, S. (1986). Flow in porous-media .2. The governing equations for immiscible, 2-phase flow. *Transport in Porous Media*, *1*(2), 105–125.

[35] S. Zahedi, K. Gustavsson, and G. Kreiss. A conservative level set method for contact line dynamics.